1-1-2007

# A computer-aided diagnosis system for lung nodule detection in pulmonary CT images based on LS-SVM and wavelet transformation

Omid Talakoub
*Ryerson University*

# A COMPUTER-AIDED DIAGNOSIS SYSTEM FOR LUNG NODULE DETECTION IN PULMONARY CT IMAGES BASED ON LS-SVM AND WAVELET TRANSFORMATION

by

Omid Talakoub
Bachelor of Electrical Engineering
Tehran Polytechnic University of Technology
Tehran, Iran, 2004

A thesis presented to Ryerson University
in partial fulfillment of the
requirement for the degree of
Master of Applied Science
in the Program of
Electrical and Computer Engineering.

Toronto, Ontario, Canada, 2007

## Author's Declaration

I hereby declare that I am the sole author of this thesis.
I authorize Ryerson University to lend this thesis to other institutions or individuals for the purpose of scholarly research.
Signature

I further authorize Ryerson University to reproduce this thesis by photocopying or by other means, in total or in part, at the request of other institutions or individuals for the purpose of scholarly research.
Signature

## Instructions on Borrowers

Ryerson University requires the signatures of all persons using or photocopying this thesis. Please sign below, and give address and date.

A COMPUTER-AIDED DIAGNOSIS SYSTEM FOR LUNG NODULE DETECTION IN PULMONARY CT IMAGES BASED ON LS-SVM AND WAVELET TRANSFORMATION

Master of Applied Science
2007

**Omid Talakoub**
Electrical and Computer Engineering
Ryerson University
Toronto, Ontario, Canada, 2007


# Abstract

One of the most important areas of biomedical engineering is medical imaging. Fully automated schemes are currently being explored as Computer-Aided Diagnosis (CAD) systems to provide a second opinion to medical professionals; of these systems, abnormal region detector in medical images is one of the most critical CAD systems in development. The primary motivation in using these systems is due to the fact that reading an enormous number of images is a time-consuming task for the radiologist. This task can be sped up by using a CAD system which highlights abnormal regions of interest. Low false positive rates and high sensitivity are essential requirement of such a system.

The initial requirement of processing any organ is an accurate segmentation of the target of interest in the images. A segmentation method based on the wavelet transformation is proposed which accurately extracts lung regions in the thoracic CT images. After this step, an Artificial Intelligence system, known as Least Squares Support Vector Machine (LS-SVM), is employed to classify nodules within the regions of interest. It is a well known fact that the lung nodules, except the pleural nodules, are mostly spherical structures whereas other structures including blood vessels are shaped as other structures such as tubular. Therefore, an enhancement filter is developed in which spherical structures are accentuated. Processing three different real databases revealed that the proposed system has reached the objective of a CAD system to provide reliable opinion for the doctors in the diagnosis fashion.

# Acknowledgments

I would like to express my gratitude to all those who gave me the possibility to complete this thesis. I would like to thank Professor Javad Alirezaie, my MASc. supervisor for his supports and encouragements through the course of my Masters study. Also I owe my most sincere gratitude to Dr. Paul Babyn, chief radiologist at Toronto Hospital for Sick Children, for providing pediatric CT images along with his detailed and constructive comments, and for his important support throughout this work.

I owe my loving thanks to my father who helped me immensely by giving me encouragement and my grateful thanks to my very close friend whose support has give me energy in the course of this research.

# Glossary

| | | |
|---|---|---|
| ARDS | ..... | *Acuterespiratorydistresssyndrome* |
| CAD | ..... | *Computer – AidedDiagnosis* |
| CT | ..... | *ComputedTomography* |
| FP | ..... | *FalsePositive* |
| GA | ..... | *GeneticAlgorithms* |
| GFV | ..... | *GradientVectorFlow* |
| HU | ..... | *HounsfieldUnit* |
| LIDC | ..... | *LungImageDatabaseConsortium* |
| LS-SVM | ..... | *LeastSquareSupportVectorMachine* |
| MRI | ..... | *MagneticResonanceImaging* |
| QP | ..... | *QuadraticProblem* |
| RBF | ..... | *RedialBasesFunction* |
| RSNA | ..... | *RadiologicalSocietyofNorthAmerica* |
| SVM | ..... | *SupportVectorMachine* |
| TN | ..... | *TrueNegative* |
| WHO | ..... | *WorldHealthOrganizations* |

# Contents

# List of Figures

# List of Tables

# Chapter 1

# Introduction

Nowadays, advancements in technology have had great impact on medical sciences. Engineering and applied sciences are leading medical sciences in examination, diagnosis and treatment of various of diseases toward faster and more accurate processes. Biomedical engineering is a broad field that connects medicine with engineering based sciences. Biomedical Engineering is a developing field that not only aims for improving the health system but also assists doctors by providing reliable data and facilitating their tasks. To satisfy these needs, Biomedical engineering has formed as integration of engineering sciences with biomedical sciences and clinical practices.

One of the most important areas of biomedical engineering is medical imaging. Over the past few years at the Annual Meeting of the Radiological Society of North America (RSNA) in Chicago, one of the major meetings in the field of diagnostic radiology, the number of papers presented on subjects related to CAD (Computer-Aided Diagnosis) has increased by approximately 50% per year, from 55 in 2000 to 86 in 2001, 134 in 2002, and 191 in 2003 [2]. The number of publications decreased after 2003 and was reported as 161 in 2004 and 163 in 2005. The majority of these presentations were concerned with three organs (chest, breast, and colon) but other organs such as brain, liver, and skeletal and vascular systems were also subjected to the CAD research. This is while the RSNA's general annual report in 2006 states that a sustaining the growth in abstract submissions has seen in recent years, RSNA received a record 10,227 abstracts for presentation consideration at RSNA 2006, 712

more than were submitted for RSNA 2005. Included were 6,838 scientific paper or poster abstracts. With the advance of computer technology, medical imaging and its automated analysis are increasingly received interest of physicians in diagnosis, treatment, and research. Fully automated schemes are currently being explored by researchers as CAD systems to provide second opinions for doctors. Many different types of CAD schemes are being developed for detection and/or characterization of various lesions in medical imaging, including conventional projection radiography, Computed Tomography (CT), Magnetic Resonance Imaging (MRI) and Ultrasound. Organs currently being targeted by CAD research include lung, breast, chest, colon, brain, liver, kidney, and the vascular and skeletal systems.

## 1.1 Computer Tomography

Computer Tomography is a noninvasive, painless medical procedure that utilizes special X-ray equipment to produce multiple images of the inside body and produce cross-sectional views of the area being studied. CT imaging is one of the best tools for study of the pulmonary and abdomen area because it provides detailed, cross-sectional views of all types of tissue. In fact CT scan reconstruct gathered data on its rotating detector to generate sequential layers of region of interest with specific axial thickness. Series of these axial layers represents a 3D view of the region or examined organ in the body. This 3D view is advantage of CT scan in comparison to traditional X-ray imaging methods on superimposing the structures due to projection of 3D structures into 2D images.

Conventional CT scanners contained a X-ray tube and a detector that rotated around the patient's body. The patient was required to suspend respiration of each scan. Then it was requisite to wait for realignment before the next scan. In recent years, advanced technology led to continues imaging and movement of the X-ray tube against the body. This system is known as helical CT. Traditional imaging devices were not even capable of scanning the region of interest since they could not move over the patient body; hence the technician should have move the patient axially in about the slice thickness and align him with center of the image. Moreover each study might have taken a tremendous amount of time to get

completed. Recently imaging techniques have been advanced much further and reached to the point where dynamic CT scanner can generate each series of images within 100ms to 200ms. This technique brings medical imaging to the point that radiologist can investigate the organ of interest over a period of time. For instance, Dynamic CT brings possibility of lung examination over several respiration cycles for a doctor.

Each material attenuates the emitted X-ray from the tube for a specific amount based on its molecular structure. The CT scanner contracts the images based on the X-ray it receives upon the detector's rotation. The Hounsfield scale is a quantitative scale for describing radiodensity which express pixel intensities in a CT image. This scale performs a linear transformation from original attenuation coefficients into a space where water is assigned to zero and air is assigned a value of -1000. Due to this mapping, Hounsfield Unit (HU) can represent ratio of air to aerated lung issue at any coordinate inside the lung in pulmonary CT images. For example, -600HU represents 60% air and 40% aerated lung tissue. Since HU spreads over quite a large range (air as average of -1000HU and bones as average of 1000HU) and usually a partial of this range receives interest, the pixel intensities are linearly windowed for visualization purposes. This window defines by its level and width. For example the lung window has width of 1500HU and level of -600HU.

## 1.2 Computer-Aided Diagnosis

The interpretation of medical images is still almost exclusively the work of humans. However, this is expected to change within the next decade due to tremendous impact of computer technology advances on medical imaging. Having computers as interpreters is called Computer-Aided Diagnosis (CAD). Although some investigators distinguish between the concepts of computer-aided detection and CAD, others have interpreted CAD broadly as encompassing both the detection task and the classification task [3]. Automatic segmentation and quantification are closely related to the CAD systems. Segmentation is needed to determine which parts of the image the computer needs to analyze and in many cases the accurate delineation of objects already yields clinically valuable information. Quantification

is often the ultimate goal of radiological examinations, once the diagnosis has been made the physician needs to determine the extent and progression of a disease. For example, examination of Acute Respiratory Distress Syndrome (ARDS) is an application of segmentation and quantification features of a CAD system.

## 1.3 Automated Lung Nodule Detection

According to the World Health Organizations (WHO), lung cancer death rate is higher than other kinds of cancers around the world since it manifests itself at an advance stage. Not smoking is considered the most effective way to reduce the incidence of lung cancer in most countries, while detection of suspicious lesions in the early stages of cancer can be considered the most effective way to improve survival [4]. Nodule detection is one of the most challenging tasks in medical image processing. Radiologists and doctors may easily miss to pick lung nodules in their early stages due to low contrast, small size, or location of the nodule within an area of complicated anatomy such as the hilum. Therefore, developing a CAD system capable of monitoring the lung and detection of its nodules seems necessary to save many lives. Pulmonary lung nodules detection has received tremendous amount of attention from researches in field of biomedical imaging and image processing in the past few years. The main goal of this system is to reliably detect nodules in patient's lung with low False Positive (FP) rate. Nevertheless, the blood vessels are often mislabeled by automated systems. A large number of false positives limits the potential usage of a detection system as an assistant to radiologists. In addition to the CAD's accuracy, multislice protocols may generate 300-600 high-resolution axial images while imaging protocol of a single detector scanners typically generates about 40 images in a pulmonary study. The large data volume is impractical to get reviewed within a proper time in a radiology practice. Therefore, efficient methods of image interpretation such as computer-assisted nodule detection are essential to detect the nodules and manage the tremendous number of studies.

### 1.3.1 Lung Nodules

In 1984, the Fleischner Society published a glossary of terms for thoracic radiology [5], in which a lung nodule was defined as

> "any pulmonary or pleural lesion represented in a radiograph by a sharply defined, discrete, nearly circular opacity 230mm in diameter."

Twelve years later, the Fleischner Society published a glossary of terms specifically for thoracic CT [6] in which a lung nodule was defined as a

> "round opacity, at least moderately well marginated and no greater than 3cm in maximum diameter."

The Fleischner Societys pathologic definition of a nodule as a "small, approximately spherical, circumscribed focus of abnormal tissue" [6] which reflects the three-dimensional nature of the physical lesion manifested radiologically as a nodule on CT scans [3]. Although these statements can be considered as well developed nodule definitions, natural complexities of biological system makes it difficult to classify a focal abnormality as nodule or other abnormalities such as scars. Therefore, providing a utilitarian definition of a nodule may not be straightforward, since the notion of a nodule may not represent a single entity capable of verbal definition. The National Cancer Institute launched a cooperative effort known as the Lung Image Database Consortium (LIDC) to develop an image database that will serve as an international research resource for the development, training, and evaluation of CAD methods in the detection of lung nodules on CT scans [3].

The appearance of pulmonary lung nodules in CT images can be described as compact lesions with attenuation near water ($\sim 0HU$). Radiologists define classes of pulmonary nodules as follows [7]:

1. Well-circumscribed: The nodule is located centrally in the lung, without significant connections to vasculature.

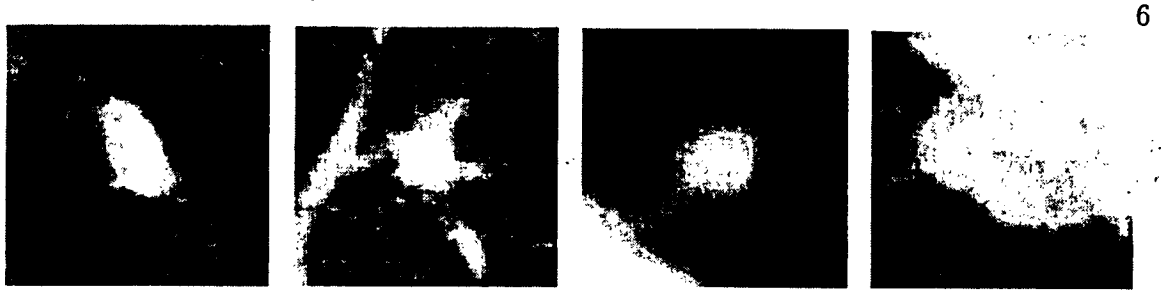


**Figure 1.1:** A typical lung nodule for each class is shown: (a) a well-circumscribed nodule. (b) a juxta-vascular nodule. (c) a nodule with a pleural tail (d) a juxta-pleural nodule [1].

2. Vascularized: The nodule is located centrally in the lung, but has significant vascularization (connections to neighboring vessels).

3. Pleural tail: The nodule is near the pleural surface, connected by a thin structure ("pleural tail").

4. Juxtapleural: A significant proportion of the nodule periphery is connected to the pleural surface.

Some examples of lung nodules are illustrated in figure 1.1. From the image processing perspective point of view, several steps should be taken to identify each class of nodule within pulmonary CT images. Several approaches have been introduced to extract each class. However, most of the proposed methods are dependent on some assumptions over the shape and appearance of lung nodules in the pulmonary CT images. For example circularity or sphericalness has been considered as one of the most important features of a well-circumscribed nodule (a brief review on proposed methods in this fashion is provided in the next chapter).

## 1.4 Contributions

The major contributions of the author in this thesis are as follows:

- Proposing a fast segmentation method based on wavelet transformation in extraction of lung in the pulmonary CT images regardless of evaluated study slice thickness (axial resolution). An algorithm for airway tree extraction is also proposed to be taken in prior to the lung segmentation in order to enhance the segmentation accuracy.

- A nodule enhancement filter is proposed as a tool to eliminate the tubular structures (vessels) in the 3D CT data. This selective filter is capable of distinguishing between spherical shape objects and tubular 3D objects (blood vessels). This filter can reduce the computation expenses of the CAD system by elimination of blood vessels in prior to the classifier module.

- A Support Vector Machine classifier is employed to extract nodules from other opacities in the lung area. This system tends to provide fairly high sensitivity in nodule detection as well as very low number of false positives per slice in compare to other proposed methods.

- Lung nodule detector CAD system is developed whose performance lies in an acceptable range to be employed in practical applications.

# Chapter 2

# Background and literature review

## 2.1 Lung Nodule Detection

Identification of potential nodule candidate in a series of images is a primary step in any nodule detection CAD system. Nevertheless, reducing number of false positive objects and pointing out the suspicious points in each slice is the most critical part of this task. Therefore emphasizing on low number of false positives and robust identification of nodule candidates are the main focuses of this chapter.

In literatures researchers utilized different methods to detect nodules in CT images. Proposed schemes for a CAD lung nodule detection are categorized into three major categories:

1. Statistical or mathematical based
2. Rule based
3. Artificial intelligence based

Not only some of the introduced methods could not detect nodules with sensitivity of higher than 70% but also the number of false positives are reported to be as high as 14 FPs per slice. Takizawa at el. [8] is introduced a 3D Markov random field to recognize pathological shadow areas inside the lung. Although Takizawa claimed that his proposed method tent to extract all the nodules with no false positive, his proposed method was studied over a small test dataset consist of 10 CT images. Unfortunately neither information on nodule types

and sizes nor its performance evaluation on a bigger database was provided. Antonelli *et al.* [9] proposed a method based on anatomical knowledge of pulmonary region. Basically the utilized CAD system tends to extract different structures within the CT images based on the volume, X-ray attenuation, and position with respect to structures already recognized. After recognition the objects inside the body, a C-Means Fuzzy algorithm was applied to classify the lung voxels into 2 clusters nodules/vessels and air. Then a neural network system came to the picture to classify nodules from this pool of ROIs. Antonelli's study lead to more than 82% sensitivity with 1.4 FPs per slice. However, it had not pointed out whether if there was any over lap between the data that neural network was trained with and the tested patients.

A small number of knowledge-based schemes are under development to automate lung nodule detection on CT [10, 11, 12, 13, 14, 15]. The major difficulty that must be tackled by these systems is distinguishing nodules from normal bronchovascular details. Bronchovascular anatomy and lung nodules have similar X-ray attenuation and appearance in individual cross-sectional CT images. Therefore, these systems do not rely solely on conventional gray level-based image processing tools. They often introduce anatomical and imaging knowledge via heuristics or rules relating to the expected attenuation, size, shape, and/or location of nodules in respect to the lung boarders as well as lung anatomy [16]. A feature-based classification approach to nodule detection has shown promising results in preliminary studies [12, 13, 14, 15]. A segmentation algorithm is applied to generate candidate nodules, then features are calculated and used to classify each candidate as nodule or nonnodule (usually a bronchovascular structure). Most features relate to size and shape on the premise that nodules are of greater diameter and tend to be spherical, while vessels are tubular. Lin *et al.* [17] processed series of images by techniques including thersholding, morphology closing, and labeling to segment the lung area and obtain the ROIs. Then, three main features, circularity, size of area, and mean brightness, are extracted from ROIs and the nodules are identified with diagnosis rules that are obtained by the neural fuzzy model. Although Lin *et al.* provided sensitivity of 89% with FP rate as low as 0.3 per image, the developed CAD missed to detect nodules bigger than 5mm or smaller than 1mm in the database with a great

rate. Giger *et al.* [12] have used multiple gray-level thresholds to extract candidates, then calculated 2-D geometric features such as perimeter, compactness and circularity for each candidate at each threshold. A rule-based approach was used to assign a confidence rating, in the range 1-5, to each 2-D candidate, with 1 being definite vessel and 5 being definitely nodule. Confidence ratings were modified based on ratings of the nodule in adjacent slices. 94% per-nodule sensitivity was achieved with 1.25 false positives (FPs) per patient. Armato *et al.* [13, 18] applied multilevel thresholding and a rolling ball algorithm towards the detection of the lung nodules. Some 3-D features such as sphericity, and gray-level features including mean and standard deviation, to classify nodules using a linear discriminant analysis were included. The algorithm achieved 70% per-nodule sensitivity with 1.5 FPs per axial section. Kanazawa *et al.* [14] segmented candidates by using fuzzy clustering to partition the histogram of pixels within the lung fields into two classes: "air part" and "blood vessels and tumors." They then used similar features in a heuristic, rule-based approach to classify nodules and vessels. These systems have been tested on limited numbers of cases with a sensitivity close to 90%, and about 20 FPs per case.

Erberich *et al.* [19] applied the Hough transform (HT) for both 2-D circles and 3-D spheres using a rule-based classifier and achieved 30%-40% per-nodule sensitivity with a "large amount of false positive nodules." Several approaches to colonic polyp CAD in CT colonography have also been proposed. Vining *et al.* [20]developed a method that measures abnormal wall thicknesses using heuristics. They reported 73% per-polyp sensitivity with a range of 9-90 FPs per patient. Other approaches have analyzed the morphology of the mucosal surface. Summers *et al.* [21, 22] have developed a method that uses size, attenuation, and curvature calculated with convolution-based partial derivatives to find polyps. They achieved 64% per-lesion sensitivity with 3.5 FPs per patient. Yoshida *et al.* [23, 24, 25] use shape index and curvedness (computed with partial derivatives), directional gradient concentration, and quadratic discriminant analysis. Using both prone and supine datasets, they achieve 100% per-patient sensitivity with 2.0 FPs per patient (per-polyp sensitivity not stated). Kiss *et al.* [26] combined surface normal and sphere fitting methods to achieve 100%

per-polyp sensitivity with 8.2 FPs per patient. In addition, secondary CAD algorithms that are designed to reduce the FP rate of primary CAD algorithms have been proposed. Gokturk *et al.* [27] applied support vector machines to shape and attenuation features to reduce FPs and reported a 50% increase in specificity at a constant sensitivity level. Acar *et al.* [28] have applied edge displacement fields to reduce FPs and reported a 23% increase in specificity at a constant sensitivity level. Both of these FP reduction methods were evaluated using initial versions [29] of the work presented in this paper.

Brown *et al.* [16] have presented an algorithm for both detection and surveillance of lung nodules in CT. Region-growing and morphological operators were used to create candidate locations. Attenuation, location, volume, and shape features were matched to model objects in a semantic net with fuzzy membership that serves as a generic a priori anatomic model. In the initial detection task, 86% per-nodule sensitivity was achieved with 11 FPs per patient. Lee *et al.* [30] used both genetic algorithm-based and semicircular template matching to identify initial candidates and attenuation, shape, and gradient feature rules to reduce FPs. They achieved 72% per-nodule sensitivity with 31 FPs per patient. Lee considered 13 features to reduce the false positives detected by template matching including Mean, Standard Deviation, Area, Circularity, Irregularity, Contrast, Max CT Value, Directional Variance, Directional Cross-Correlation of the Pixel Gradient, and Inverse Difference Moment. Lee's method still has difficulty to detect low-contrast nodules and those in the apex and basis pulmonis effectively. Dehmeshki *et al.* [31] significantly improved the performance of GA nodule detection CAD system by combining local shape feature calculation into global cross-correlation framework for Genetic Algorithm Template Matching. Nodules can still be missed if there are no spherical local elements or the size of the elements is not matching to any of the templates. Feature extraction is one of the most important steps in machine learning-based FP reduction, as features must have sufficient discriminatory power to distinguish nodules from nonnodules. Boroczky *et al.* [32] proposed a feature subset selection method using Genetic Algorithms (GAs) to automatically determine the optimal size of the feature subset, and also choose the most relevant features from the feature pool.

The optimal feature subset is used to train a classifier based on SVMs that classifies detected structures into true and false nodules. The proposed method tent to reduce the false nodule rate up to 50% while retaining the same sensitivity. Diccioti *et al.* [33] proposed a semi-automatic method for 3D segmentation of lung nodules in CT images for subsequent volume assessment. The distinguishing features of his algorithm were 1) the user interaction process which allows the introduction of the knowledge of the expert in a simple and reproducible manner. 2) the adoption of the geodesic distance in a multi-threshold image representation. It allows the definition of a fusion-segregation process based on both gray-level similarity and shape. The algorithm was validated on low-dose CT scans of small nodule phantoms (mean diameter 5.3-11mm) and in-vivo lung nodules (mean diameter 5-9.8 mm) detected in the Italung-CT screening program for lung cancer. The main weakness of Diccioti method over many other proposed methods is its dependency on user interaction on its process since the overall reported performance is in the range of other fully automated methods. There are many problems in which the traditional rule based approaches can not provide satisfactory result. Image processing applications in which the object is changed temporally and computationally expensive cases are examples of this class of problems. Scientists arise an alternative strategy for these types of situation in which the computer struggles to learn the input and output relationships from the examples. The approach of synthesizing a model based on provided examples is known as learning. In a more advanced fashion the examples are formed as pairs of input and output, also known as supervised learning. This learning concept is derived from human learning pattern in which the individual tries to generalize his understanding over a specific concept such as classification by looking at some examples.

## 2.2 Artificial intelligence and lung nodule detection

A Considerable number of studies on lung nodule detection have been employed artificial intelligence including neural networks [34, 35, 9], LDA [36], and SVM to detect lung nodules or reduce the number of false positives. It has been reported in many literatures that Support Vector Machine (SVM) outperforms other artificial intelligence systems including

neural networks when it comes to the lung nodule classification in the thorax CT images.

Support Vector Machine (SVM) initially was proposed as classifier for the binary cases. A binary case is a problem in which the test data gets separated into two major groups. For instance as interest of this thesis, each voxel in a series of CT images taken from each individual can be classified as focal abnormality/nodule or non-nodule voxels. While most engineers are aware of weaknesses and strengths of many of the existing methods including neural network, fuzzy logic, time series and stochastic models, the introduction of an innovative learning machine by Vapnik [37] brought a new solution to some of the others shortcomings in various applications. Support Vector Machine came into sight of researchers as combination of statistical learning theory and structural risk minimization principle. Structural risk minimization offers a structured foundation to avoid over fitting due to complexity of the model while statistical learning causes generalization of the SVM scheme.

Advantages of support vector machine over other artificial intelligence schemes such as neural networks have been reported by many literatures. Indeed, SVM was employed for isolated handwritten digit recognition, object recognition, speaker identification, face detection in images, text recognition, etc. It has received an increasing attention for pattern recognition. For example, traditional neural network approaches have faced difficulties with finding a general model to fit any data. This difficulty is removed when the problem is solved using SVM PI. Nevertheless, the performance of support vector machine is highly dependent on the choice of the mapping function and feature selection suitable to the problem in hand. Therefore, a SVM algorithm designed for a specific problem may not offer acceptable result to other problems. Malone *et al.* [38] proposed a method to classify a CT image's pixel into 4 group of body, normal, fibrosis and Emphysema regions. Malone achieved accuracy of 92% as a result of processing 102 images in their study. Mousa and Khan [39] attempted to classify the lung nodules by utilizing SVM as the classifier. Although Mousa and Khan reached to 87.5% sensitivity in their study, a small cropped partial of pulmonary images was presented to the learner algorithm; hence the learner just dealt with close up image of nodule or non-nodule objects in this study. However, Mousa and Khan outperformed previously

reported studies based on neural networks such as the study done by Penedo *et al.* [40] in which 90 real nodules and 288 simulated nodules were used for the training, and then the system was tent to provide 89% - 96% sensitivity.

# Chapter 3

# Support Vector Machine schemes

The main aspect of SVM is mapping the data space into a higher dimensional space in order to construct a hyperplane as the decision surface such that the separation margin between the classes is maximized. For example in separable classification cases, SVM tries to transform the input data space into a space where classes are separated by hyperplanes. Based on this, SVM is categorized under supervised learning artificial intelligence group. SVM attempts to transform the input space by an estimated function into a higher dimensional space where the relationship between input and output is as linear as possible. This involves solving a Quadratic Problem (QP) with a unique global minima, while gradient based training methods of neural network architectures suffer from existence of many local minima.

The learning schemes also are categorized into two major groups based on their capability on utilizing the presented training data. The first type is batch learners in which all the training data would be presented to the learner when the learning process commences. The second group is known as online learners who are capable of learning gradually and updating their parameters over the time. Online learning schemes are showing their advantages in the cases where the training data comes continually over the time or in nonstationary environments. SVM and LS-SVM (Least Square Support Vector Machine) are categorized under online learning models. This property of support vector machines is suitable for the lung nodule detection applications since the classifier can be updated at any time with new nodules or false positive examples as needed. Furthermore using learning machines in such

an application offers a general implementation; hence the developed software does not need to be modified based on the input images acquired conditions such as X-ray dose.

As pointed out earlier support vector machines are powerful schemes on pattern recognition and classification problems. Due to SVM capability and high sensitivity of SVM structure in these kinds of problems, researchers attempt to modify and expand this theory to suite it to their problems. Least Squares Support Vector Machines (LS-SVM) are simplified version of SVMs since LS-SVM considers equality constraints for the classification problem directly from solving a set of linear equations, instead of quadratic programming [41]. Therefore, SVM is described in prior to the LS-SVM classifier. The ability of algorithm to accurately perform the transformation and classify any data outside of the training data is known as generalization. Generalization property shall be optimized based on the application and nature of processed data.

Having advantages of support vector machines in mind and considering nature of the tackled problem in this thesis, support vector machine model is chosen as the classifier to exploit the task on detection of a pulmonary focal abnormalities subcategory known as nodule.

## 3.1 Support Vector Machines

Support Vector Machines can be categorized into 2 major groups as linear and nonlinear classifiers. In practical problems, the input classes are unlikely to be linearly separable, so non-linear SVM models are usually utilized in the real life problems. Therefore, non-linear support vector machines are described and linear SVMs are not included in the outline of this thesis. Non-linear SVM models are inspired by Cover theory which states that a linearly non-separable pattern space can be transformed into a new feature space where patterns are linearly separable with a high probability. Based on this theory, not only the transformation should be non-linear but also the feature space dimension should be high enough to provide the linear separation between the classes. SVM employs a hypothesis space of linear function in a high dimensional feature space, trained with learning algorithm. The learning algorithm

is derived from optimization theory and implements a learning bias derived from statistical learning theory.

To put this into a mathematical format, lets assume a training set of input and output patterns consist of $N$ points is given. Then the decision surface is defined as a hyperplane formulated as

$$\sum_{j=1}^{N} \mu_j y_k \Psi(x, x_j) + \beta = 0 \tag{3.1}$$

where $x_k \in R^n$ is the $k$-th input pattern, $y_k \in R$ is the $k$-th output pattern, $\{\mu_j\}_{j=1}^{N}$ are positive real constants denoting a set of linear weights and $\beta$ is a real number known as bias. $\Psi(x, x_j)$ typically is chosen as $x_j x$ for linear SVM; $(x_j^T x + 1)^d$ for polynomial SVM of degree $d$; $e^{-\|x-x_j\|_2^2/\sigma^2}$ for Redial Basis Function SVM; $tanh[\kappa\, x_j^T x + \theta]$ for MLP SVM. This equation can be rewritten as

$$\sum_{j=0}^{N} \mu_j y_k \Psi(x, x_j) = 0 \tag{3.2}$$

where $\Psi(x, x_0) = \beta$ and $\mu_0 = 1$. The classifier is constructed as

$$y_j(w\varphi(x_j) + \beta) > 0,\ j = 1, ...., N \tag{3.3}$$

where $\varphi(.)$ is a nonlinear mapping function between input and higher dimensional feature space defined as $\varphi(x)^T \varphi(x_k) = \Psi(x, x_k)$. In case where a separating hyperplane in the feature space does not exist, the problem of finding weights $w$ would be reformed to risk minimization problem by formulating the optimization problem:

$$\begin{cases} \min_{w,\xi_j} \lambda(w, \xi_j) = \frac{1}{2} w w^T + c \sum_{k=1}^{N} \xi_k \\ \xi_k \geq 0 \end{cases} \tag{3.4}$$

Therefore the Lagrangian is constructed as follows:

$$L(w, \beta, \xi_k; \mu_k, v_k) = \lambda(w, \xi_k) - \sum_{k=1}^{N} \mu_k \{y_k[w\varphi(x_k) + \beta] + \xi_k\} - \sum_{k=1}^{N} v_k \xi_k \tag{3.5}$$

where $\mu_k \geq 0$, $v_k \geq 0$ $(k = 1, \ldots, N)$ are Lagrange multipliers. The solution to constrained optimization problem is determined by the saddle point of the Lagrange function $L(w, \beta, \xi_k; \mu_k, v_k)$, which has to be minimized with respect to $w$ and $\beta$. It also has to be

maximized with respect to $\mu$.

$$\max_{\mu_k, v_k} \min_{w, \beta, \xi_k} L(w, \beta, \xi_k; \mu_k, v_k) \tag{3.6}$$

which leads to this set of equations

$$\begin{cases} \frac{\partial L}{\partial w} = 0 \rightarrow w = \sum_{k=1}^{N} \mu_k y_k \varphi(x_k) \\ \frac{\partial L}{\partial \beta} = 0 \rightarrow \sum_{k=1}^{N} \mu_k y_k = 0 \\ \frac{\partial L}{\partial \xi_k} = 0 \rightarrow 0 \leq \mu_k \leq c, \qquad k = 1, \ldots, N \end{cases} \tag{3.7}$$

which leads to solving a quadratic programming problem

$$\max_{\mu_k} Q(\mu_k; \varphi(x_k)) = -\frac{1}{2} \sum_{k,l=1}^{N} y_k y_l \varphi(x_k)^T \varphi(x_l) \mu_k \mu_l + \sum_{k=1}^{N} \mu_k \tag{3.8}$$

or

$$\max_{\mu_k} Q(\mu_k; \Psi(x_k, x_l)) = -\frac{1}{2} \sum_{k,l=1}^{N} y_k y_l \Psi(x_k, x_l) \mu_k \mu_l + \sum_{k=1}^{N} \mu_k \tag{3.9}$$

such that

$$\begin{cases} \sum_{k=1}^{N} \mu_k y_k = 0 \\ 0 \leq \mu_k \leq c, \qquad k = 1, \ldots, N \end{cases} \tag{3.10}$$

Since the matrix associated with this quadratic problem is not indefinite, the solution to equation 3.9 is global [42].

## 3.2 Least Squares Support Vector Machine scheme

One of the main applications of nonlinear SVMs is solving the nonlinear classification problem by means of convex quadratic programs. Recently, the Vapnic formulation has been modified in order to be transformed into a set of linear equations instead. It makes it much easier to be used in the practical fashions. The original aspects of this idea were introduced by Suykens [43]. The Vapnik formulation was modified at two points. First, Suykens changed inequality constraints with qualities. This modification changes the constrain from a threshold value to a target value. Upon introducing a target value misclassifications are allowed to be tolerated in case of overlapping distributions. Second, a new squared loss function can be

defined based on the constraint error variable. These two modifications simplify solving the nonlinear classification problems in addition to classifier parameters determination. To introduce Least Squares version of Support Vector Machine classifiers equation 3.4 should be rewritten as

$$\min_{w,\beta,e} \lambda(w,b,e) = \frac{1}{2}ww^T + \gamma\frac{1}{2}\sum_{j=1}^{N} e_j^2 \tag{3.11}$$

$$y_k[w^T\varphi(x_j)+\beta] = 1-e_j, \qquad j=1,\ldots,N \tag{3.12}$$

$$L(w,\beta,e;\mu) = \lambda(w,b,e) - \sum_{j=1}^{N}\mu_j\{y_j[w^T\varphi(x_j)+\beta]-1+e_j\} \tag{3.13}$$

The conditions for optimality

$$\begin{cases} \frac{\partial L}{\partial w}=0 \rightarrow w=\sum_{k=1}^{N}\mu_k y_k\varphi(x_k) \\ \frac{\partial L}{\partial \beta}=0 \rightarrow \sum_{k=1}^{N}\mu_k y_k=0 \\ \frac{\partial L}{\partial e_k}=0 \rightarrow \mu_k=\gamma e_k, \qquad k=1,\ldots,N \\ \frac{\partial L}{\partial \mu_k}=0 \rightarrow y_k[w\varphi(x_k)+\beta]-1+e_k=0, \qquad k=1,\ldots,N \end{cases} \tag{3.14}$$

which can be written in a matrix form of:

$$\left[\begin{array}{ccc|c} i & 0 & 0 & -Z^T \\ 0 & 0 & 0 & -Y^T \\ 0 & 0 & \gamma^I & -I \\ \hline Z & Y & I & 0 \end{array}\right]\left[\begin{array}{c} w \\ b \\ e \\ \hline \mu \end{array}\right] = \left[\begin{array}{c} 0 \\ 0 \\ 0 \\ \hline \vec{1} \end{array}\right] \tag{3.15}$$

Where $Z=[\varphi(x_1)^T y_1;\ldots;\varphi(x_N)^T y_N]$, $Y=[y_1,\ldots,y_N]$, $\vec{1}=[1;\ldots;1]$, $e=[e_1;\ldots;e_N]$, $\mu=[\mu_1;\ldots;\mu_N]$. Following linear Karush-Kuhn-Tucker system leads to elimination of $w$ and $e$ [42, 44]:

$$\left[\begin{array}{c|c} 0 & y^T \\ \hline y & \Omega+I/\gamma \end{array}\right]\left[\begin{array}{c} b \\ \hline \alpha \end{array}\right] = \left[\begin{array}{c} 0 \\ \hline \vec{1} \end{array}\right] \tag{3.16}$$

Where $\Omega = Z^T Z$; hence the classifier dual space takes the form of

$$y(x) = sign\left[\sum_{k=1}^{N}\alpha_k y_k K(x,x_K)+b\right] \tag{3.17}$$

It should be noted that the solution can be expressed in terms of the error variable $e$ by elimination of $\alpha$ instead of $e$ from the equation 3.14. Also chosen kernel function, $K(x,x_k)$, must be positive definite and Mercer condition, [45]:

$$\int\int K(x,y)g(x)g(y)dxdy \geq 0 \tag{3.18}$$

Selection of a positive definite kernel of $K(.,.)$ guarantees that the matrix introduced in the QP is positive definite (all eigenvalues are strictly positive) [42]. Hence, $K(x,y)$ can be expressed as the auto-inner product of a function, $\varphi(x)^T\varphi(y)$. The dual of LS-SVM is obtained by solving the equation 3.16 which is a square system with an unique answer if the matrix has full rank.

Redial Bases Function (RBF) kernel, $K(x,x_k) = exp(-||x-x_k||^2/\sigma^2)$, is chosen as the kernel function in this thesis due to its nonlinear characteristic and reported performance on nonlinear classification problems. Although solution of the linear system (3.16) results only on determination of $\alpha$ and $b$, there are several ways to determine the kernel parameters including $\sigma$. One of the simplest and the most time-consuming ways is to work on a training, validation and test set, by evaluation of the possible combinations of $\sigma$ and $\lambda$. Then pick the values that give the best performance on the validation set. However, the outcome might be too sensitive to the chosen sets. Therefore, it is statistically better to chose N-folded cross-validation sets regardless of its heavier computational order. Other alternatives are determination of hyperplane parameters by Bayesian inference and bootstrap techniques. In order to reduce the computational expense and increase the speed of the CAD system, Baysian inference method is employed to determine the optimal parameters of the classifier.

# Chapter 4

# Lung Segmentation and Lung Nodule Enhancement Filter

## 4.1 Lung Segmentation

Image segmentation is concerned with the partition of pixels into regions of uniform properties. In the simplest case, it means to distinguish objects from the backgrounds. In other words, segmentation subdivides an image into its constituent regions or objects [46]. The first step in examining any organ in a study is segmentation/extraction of particular organ in series of images. Segmentation accuracy highly affects CAD system performance since any segmentation error may lead to misdiagnosis. Several methods have been utilized to segment the lung in pulmonary CT images such as thresholding [47], watershed [48], snakes [49], and region growing [50]. A segmentation technique is proposed that outperforms the above-mentioned techniques.

### 4.1.1 Thresholding

Thresholding is the most popular lung segmentation method due to its simplicity in methodology and computation. This methodology based on an assumption that the most lung tissue will appear in the range of -910HU to -500HU in the CT images, while the chest wall, blood, and bone will be much more denser (well above -500HU). The main goal of this methodology is focused on finding a threshold value that separates the pixels corresponding to the lung tissue from the pixels corresponding to its surrounding tissues. Conventional methods

attempt to find a fix global threshold value. On the other hand more recent methods tend to look for local or optimal threshold value(s) in each image rather than dealing with globally defined value(s) . Optimal thresholding is an automatic threshold selection method that allows accommodation of small variations in tissue density expected across a population of subjects. Optimal thresholding utilizes sequence of iterations in order to find the optimal value in an image. It categorizes each pixel as body and non-body (lung) pixels. Usually this method updates its threshold value as the soft tissues and the lung average intensities. Although thresholding holds a relatively simple idea behind, a lot of post processing steps, including Connectivity and Topological Analysis, Segmentation of the Large Airways, and smoothing ,are required to eliminate the misregistration of the extracted lung area in a pulmonary CT image [47]. Despite all these efforts, thresholding has many short comings in segmenting of the lung in CT images. It has faulty segmentation result such as missing boundaries between 2 regions when the gray-level of boundary's intensity do not differ significantly. For example, this method merges the left and right lung or artifacts caused by airways. In addition, CT lung density is influenced by factors such as subject tissue volume, air volume, image acquisition protocol, physical material properties of the lung parenchyma, and degree of inspiration. These factors make the selection of a single gray-level segmentation threshold value challenging and also several threshold values are likely to be required to extract different objects.

### 4.1.2 Region growing and Active Contour schemes

Snakes or active contour models are curves defined within an image domain that can reform under influence of the curves by themselves and the image features. Impact of curve parameters on Snakes evolution is defined as internal energy whereas impact of image features such as edges is defined as external energy. This model utilizes a closed contour to approach object boundary by iteratively minimizing its energy function, which lead to its conformation to the object boundary or other desire features within the image. Snakes are widely used in many application including edge detection, shape modeling, segmentation, and motion

tracking in the medical imaging field.

Region growing scheme is well-known for providing a good estimation of object shape and boundaries. The basic idea of this method is to initiate from a given starting point (seed) and grow as a region where its pixels satisfy an homogeneity criterion. The criterion for homogeneity is usually based on image intensity. Obviously, with this intensity-based region growing, it is very difficult to segment connected structures with similar intensities.

One of the drawbacks of traditional snake model is that the construction of initial contour often requires human interaction and the segmentation results may be heavily sensitive to initial contour conditions. It is laborious for users to draw a contour near the object boundary. However, if the initial contour is far from true object boundary, the result will not be accurate. In automated systems, a challenging issue is to choose robust seed points/region without user interaction. An important issue for dependent CAD system to region growing is how to choose the seed without the interaction of users. This issue led researchers in deploying parametric and non-parametric algorithms. There are two key difficulties with parametric active contour algorithms. First, the initial contour must, in general, be close to the true boundary or else it will likely converge to the wrong result. Several methods have been proposed to address this problem including multiresolution methods, pressure forces, and distance potentials. The basic idea is to increase the capture range of the external force fields and to guide the contour toward the desired boundary. The second problem is that active contours have difficulties progressing into boundary concavities. There is no satisfactory solution to this problem, although pressure forces, control points, domain-adaptivity, directional attractions, and the use of solenoidal fields have been proposed. However, most of the methods proposed to address these problems solve only one problem while creating new difficulties. For example, multiresolution methods have addressed the issue of capture range, but specifying how the snake should move across different resolutions remains problematic. Another example is pressure forces, which can push an active contour into boundary concavities. However, these forces can not be too strong otherwise weak edges will be overwhelmed [51]. Pressure forces must also be initialized to push out or push in, a condition that man-

dates careful initialization. Several proposed studies utilized pre-processing algorithms such as evaluating threshold value(s) [49] or Gradient Vector Flow (GFV) [50] to obtain some proper seeds inside the lung. Although GVF is less sensitive in initial contour conditions, it still needs manual drawing and can not process multiple objects simultaneously. Gradient Vector Flow is a new class of external forces used for active contour models that addresses both problems listed above. These fields are dense vector fields derived from images by minimizing a certain energy function in a variational framework. However, GVF does not provide acceptable performance when it comes to segmentation of unhealthy lung such as a lung affected by ARDS.

### 4.1.3 Watershed Transformation

Watershed algorithm is a powerful region-based method that can be used to segment images without initial contours and user interaction. Researchers use this method due to nature of pulmonary CT images that most part of the lung has intensity of lower than -500HU whereas body tissues are represented well above -500HU in the images. Watershed picks the same aspect in order to partition the image into segments in a sense that it uses the gray-level difference between the segments in order to create a continuous border between them by morphological operators. The concept of watershed is based on visualizing the image as a topological structure, in which the gray levels are considered as height. This method is based on the phenomenon observed in geography that when the water is flooding up in an area with hills and valleys, the water floods up from the lowest valleys. When the water in the neighboring two valleys merge, the borders between the valleys can be detected. Vincent and Soille proposed a modified version of the watershed method to speed up the computation [52]. The input pixel values are first sorted so that pixels in the same gray level can be accessed more efficiently. The flooding step is processed and different regions are labeled. The image is then segmented into many small regions and finally a region merging step is proceeded to acquire meaningful objects out of enormously small segments. Furthermore Yu and Chiang [48] proceed to the pixel-labeling procedure based on anatomical homogeneity

(a) (b) (c)

**Figure 4.1:** (a) Original Thoracic CT image (b) Gradient edge detector (c) Sobel edge detector.

precisely for pulmonary CT images.

Watershed tend to have relatively low computational cost. However, *over-segmentation* is a well-known drawback of watershed transformation. Utilizing marker-based watershed transformation is suggested to overcome over-segmentation in processing of medical images. Additionally, the result of watershed transformation in pulmonary CT images segmentation should be post-processed to include some dense structures such as hilar vessels.

### 4.1.4 Edge Detection by Wavelet Transformation

Edge information in images is an important characteristic of images content. Conventional edge detection algorithms, such as the Sobel, Prewitt, and Roberts operators, are typically based on differential operators. Traditional differential operators work well with edge detection of noiseless images. Nevertheless, they may miss the edges or detect false edges in the presence of noise due to their high level of sensitivity to the noise and existence of tiny intensity discontinuities in the medical images. Results of gradient and Sobel of edge detectors are illustrated in figure 4.1; edge detectors do not perform well on this image even though the noise is relatively low.

Witkin[53] introduced theory of using the scale space correlation of the subband decompositions of a signal to filter noise from the signal. His algorithm was developed to track major edges in a signal from coarse scales to fine scales in the subband decompositions and

was able to distinguish major edges from noise background at finer scales. Mallat *et al.* [54] introduced a complete signal representation by wavelet transform as special case of subband decompositions. They distinguish edge maxima from noise maxima by analyzing the singularity properties of wavelet transform domain maxima across the various scales [55]. Several studies examined de-noising of the MRI images based on a same methodology. Xu *et al.* [56] performed wavelet transformation domain filter to de-noise MR head images with 12dB SNR. Their approach to filtering of the noise from a signal also relies on the variations in scale of the wavelet transform data of the signal, but rather than detecting edges directly on the wavelet transform data with a complicated algorithm, such as those introduced in [53] and [55], they use the direct multiplication of wavelet transform data at adjacent scales to distinguish important edges from noise and accomplish the task of removing noise from signals. Karras and Mertzios [57] proposed edge detection in MRI images as combination of wavelet transform and neural network (k-level 2D wavelet transform applied to sliding windows raster scanning the original image as well as on Vector Quantizing Self-organizing Feature Maps (SOFW and SVD analysis)).

## 4.2 Wavelet Edge Detectors

Points of sharp variations are often among the most important features for analyzing the properties of transient signals or images. They are generally located at the boundaries of important image structures. Conventional edge detection algorithms are typically based on differential operators, such as the Sobel, Prewitt, and Roberts operators. Traditional differential operators work well with edge detection of noiseless images. But in the presence of noise they may miss the edges or detect false edges due to their high level of sensitivity to noise and existing of tiny intensity discontinuities in medical images. As addressed in [56] and [58], wavelet expansion in higher scales suppress effect of noise on edge detection process. Due to this advantage, several algorithms addressed the edge detection of noisy signal or images [56, 58, 59, 54, 60]. Medical images are noisy in nature due to limitations of imaging techniques, device noise and health constraints (such as giving minimal possible radiation

doses to patients). De-noising as preprocessing step is recommended in CAD systems even though de-noising may suppress some important image edge details. Therefore, algorithms with low sensitivity to noise tend to give higher performance in medical images processing problems. Wavelet transformation can be developed in a way that it preserves the significant singularities along the scales and vanishing other singularities by moving through the scales as described in details at [59, 54, 60].

Aerated lung pixels have extremely different intensity compared to other surrounding body tissues. Therefore, lung borders would be illustrated as significant discontinuities. In other words, the significant discontinuities in a thoracic images occur along lung and body borders because of large difference in HU values between two border sides (one side is soft tissue with well above -500HU whereas other side has lower CT values with a mean intensity close to air, -1000HU). A wavelet-based method that can overcome these issues and extract actual lung edges in a pulmonary CT image is proposed.

### 4.2.1 Wavelet Transformation

Wavelet transformation represents a signal or an image in multi-scale details by applying a basis function, also known as mother wavelet, to the signal. Wavelet transformation on 1D space is described in this section without loosing any generality, and then it is expanded to higher dimensions. Wavelets are families of functions $\Lambda_{s,t}(x)$ generated from a single mother wavelet, $\Lambda(x)$, by dilations and translations

$$\Lambda_{s,t}(x) = \frac{1}{\sqrt{|s|}}\Lambda(\frac{x-t}{s}), \tag{4.1}$$

where $s$ is the dilation (scale) parameter, and $t$ is the translation parameter. Mother Wavelet must have a mean of zero, and the useful ones have localized support in both spatial and Fourier domains. Wavelet transformation of a signal, $f(x)$, is defined as convolution of mother wavelet with the signal.

$$W_s^f = \Lambda_{s,t}(x) * f(x) \tag{4.2}$$

*where,*

$$f(x) * \Lambda_{s,t}(x) = \int_{-\infty}^{+\infty} f(x-\beta)\frac{1}{\sqrt{s}}\Lambda(\frac{\beta-t}{s})d\beta$$

Based on the definition of wavelet transformation (equation 4.2), the wavelet transform is capable of providing the spatial and frequency information simultaneously. Since designed wavelet transformation must detect the edges in an image which is one the main goals of this thesis, $\Lambda(x)$ is chosen as derivative of a smoothing function $\theta(x)$. Having exploited $\Lambda(x)$ as such a function turns equation 4.2 into

$$\begin{aligned} W_s^f &= (\frac{\partial}{\partial x}\theta(x)) * f(x) \\ &= \frac{\partial}{\partial x}(\theta(x) * f(x)) \end{aligned} \tag{4.3}$$

where $\theta(x) * f(x)$ smooths the signal and suppresses the noise in prior to applying the derivative operator. Consequently, detected false edges in conventional derivative based method, as shown in figure 4.1, would be eliminated automatically. Smoothing function is any function $\theta(x)$ whose integral is equal to 1 and that converges to 0 at infinity. In the particular case where $\theta(x)$ is a Gaussian, the zero-crossing detection is equivalent to a Marr-Hildreth [61] edge detector, whereas the extrema detection corresponds to a Canny [62] edge detector. Choosing a proper smoothing function that represents a low pass filter in Fourier domain when the scale $s$ is large enough, the convolution with $\theta_s(x)$ removes small signal fluctuations; therefore only sharp variations of large structures are detected. Figure 4.2 shows a horizontal profile taken from an original CT thoracic image. In this experiment the smoothing function is taken as Gaussian function. The significant discontinuities in this profile occur at the edges, while the small spikes in its horizontal profile represent image noise and slight changes in body tissues or small objects in the image including small vessels or bronchi. As illustrated the significant edge (lung border) are preserved through the scales while low inflections fade away when scale increases. Figure 4.2 shows a horizontal profile taken from a row of an original CT thorax image. The significant discontinuities in this profile occur at the edges, while the small spikes in its horizontal profile represent image noise and slight changes in body tissues or small objects in the image including small vessels or bronchi.

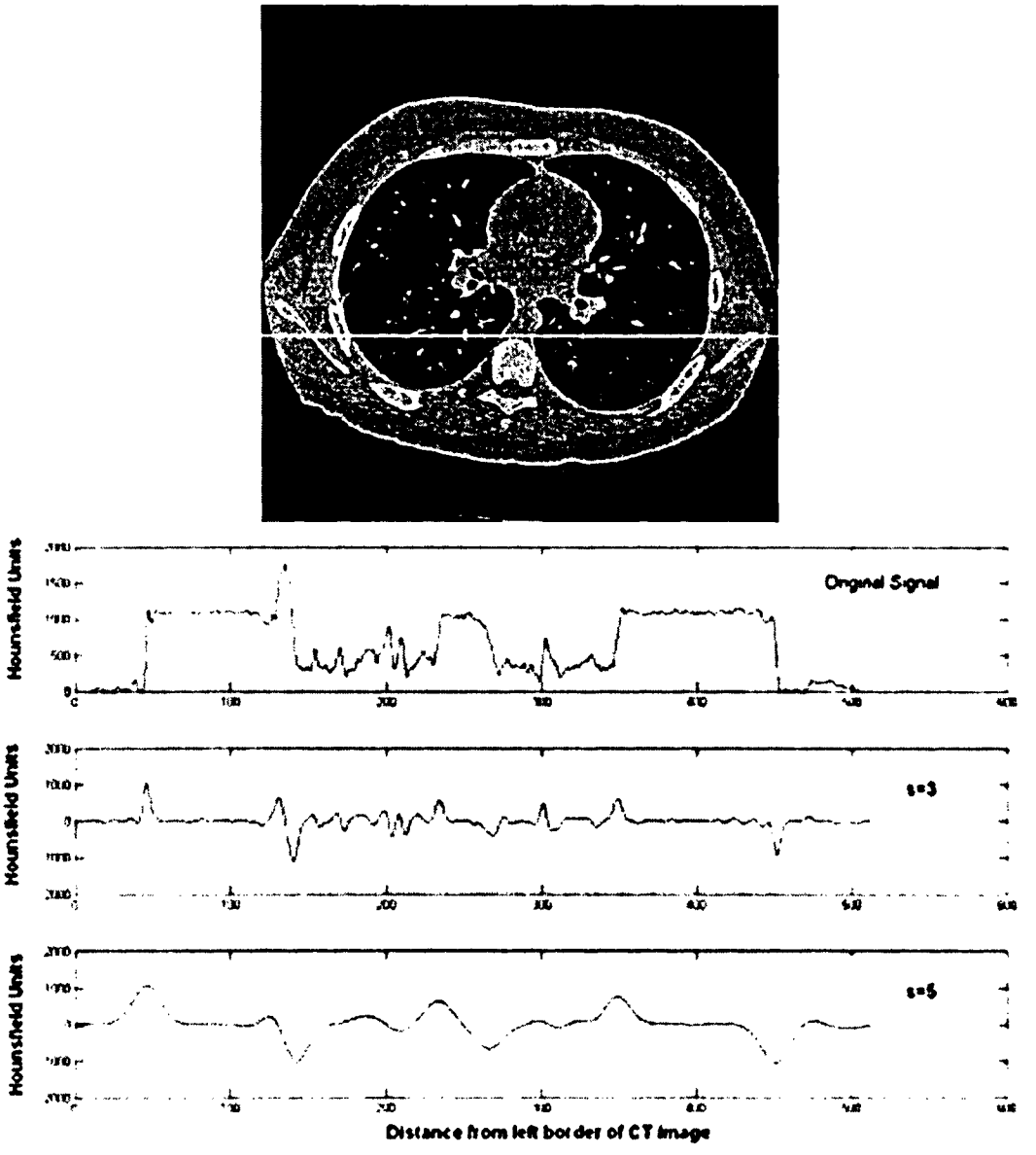


Figure 4.2: Horizontal profile (shifted by 1024HU) of lung in a CT image at the top along with its wavelet transformations in dyadic sequence below

The term 2D smoothing function is used to describe any function $\theta(x,y)$ whose integral over $x$ and $y$ is equal to 1 and converges to 0 at infinity. An image $f(x,y)$ is smoothed at different scales '$s$' due to getting convoluted with $\theta(x,y)$. When the scale '$s$' is high enough, the convolution with $\theta_s(x,y)$ removes small signal fluctuations; therefore only the sharp variations will become maxima of wavelet transformation. Image edges are defined as points $(x_0,y_0)$ where the modulus of the gradient vector is maximum in the direction towards which the gradient vector points in the image plane. In other words, edge points are inflection points of the surface $\nabla(f*\theta_s)(x,y)$. The direction of the gradient vector, $\nabla(f*\theta_s)(x,y)$, at a point $(x_0,y_0)$ indicates the direction in the image plane $(x,y)$ along which the directional derivative of $f(x,y)$ has the largest absolute value. Two wavelet functions $\Lambda_s^1(x,y)$ and $\Lambda_s^2(x,y)$ were defined such that

$$\begin{aligned} \Lambda_s^1(x,y) &= \frac{\partial\theta_s(x,y)}{\partial x} \\ \Lambda_s^2(x,y) &= \frac{\partial\theta_s(x,y)}{\partial y} \end{aligned} \tag{4.4}$$

The wavelet transform of $f(x,y)$ at scale '$s$' has two components, $W_s^1 f$ and $W_s^2 f$, defined as

$$\begin{aligned} W_s^1 f(x,y) &= f*\Lambda_s^1(x,y) \\ W_s^2 f(x,y) &= f*\Lambda_s^2(x,y) \end{aligned} \tag{4.5}$$

Then absolute magnitude and angle of wavelet transformation at each point is defines as

$$|W_s f(x,y)| = \sqrt{W_s^1 f(x,y)^2 + W_s^2 f(x,y)^2} \tag{4.6}$$

$$\angle W_s f(x,y) = \tan^{-1}\frac{W_s^2 f(x,y)}{W_s^1 f(x,y)} \tag{4.7}$$

Usually, the wavelet model is not required to keep a continuous scale parameter '$s$'. To allow fast numerical implementations, Mallat and Zhong[60], imposed that the scale can only vary along the dyadic sequence $(2^j)_{j\in Z}$. Noise filtration and elimination of low inflection points in the transformed image upon applying the wavelet is performed based on the fact that sharp edges have large amplitude over the dyadic scales $(2^j, j=0,1,2,...)$, and noise

dies out swiftly while '$s$' increases. The wavelet transform content at several adjacent scales was used to accurately detect the location of edges and some other fine details.

### 4.2.2 Proposed Wavelet Transformation

As described in section 4.2.1, many researchers tend to utilize a mother wavelet as first derivative of a smoothing function, usually a Gaussian function. On the other hand, second derivative of a smoothing function can be chosen as the mother wavelet. In this case, wavelet transformation will represent smoothed Laplasian image; hence zero crossings of the transformation can be considered as the edge locations. Despite lower computational expenses, depending on zero crossing offers many false edges since any inflection point of smoothed image can generate a zero crossing in the Laplasian image. Therefore, information about zero crossing should be post processed in order to eliminate those false alarms. A wavelet transformation is proposed as combination of first and second derivative of a proper smoothing function for pulmonary CT images. Since the proposed wavelet transformation combines first and second derivative of smoothed images, it provides faster and more accurate result than other methods. Furthermore, the computational expenses can be reduced by implementation of fast wavelet transformation proposed by Mallat *et al* [60].

## 4.3 Central Airway Extraction

In some slices the distance between bronchi and lung wall is 2 pixels; for instance right before bronchi enters the lung area (figure 4.3). Such a close distance between bronchi and lung wall will affect edge detection procedure since the tissue between them has quite the same profile as vessels or further bronchi generations. Therefore, trachea and main bronchi have been extracted prior to performing the edge detection on series of CT images.

A 3D region growing method is proposed in order to segment trachea in CT image. This method is based on the fact that the air trapped inside the trachea appears with mean density of -1000HU while the trachea wall intensity is in range of body soft tissues. Therefore, a 3D region growing method would be able to start from a seeding point inside the trachea

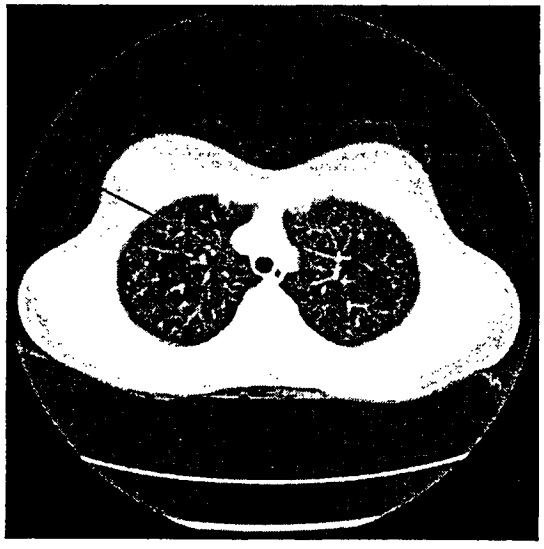

**Figure 4.3:** Trachea is located within 3 pixels of lung border.

and grow inside it to the end of primary bronchi where the bronchi tree has entered into the lungs. The CT images studied in this thesis are acquired from children in age of 5 to 15 with slice thickness of $5mm$. These thick slices cause the tree to look disconnected from an image to the consequent one due to large displacement of bronchia tree from a slice to adjunct slices. Therefore, conventional region growing methodology should be modified. Especially close to second branchia branches where these displacements are increased to such an extend that air way tree in consecutive slices may not overlap at all. In case of occurrence of this phenomenon, the proposed region growing scheme will find the initial seed in the next slice by searching the extracted region neighborhood area in 150% size of bronchi in the current slice. Then each region of interest will be verified based on its profile and size. The remaining part is to automatically find a seeding point inside the trachea. For locating the first seeding points, trachea extracted from the highest slice by wavelet edge detection described in section 4.2.1 is used. Then center of trachea would be used as the seed point for the next slice till algorithm reaches bifurcation. For the slices lower than bifurcation, overlap between locations of currently extracted bronchi and low HU values would be considered as candidates of bronchi regions. Result of this process on a series of CT images is shown in

figure 4.5.

## 4.4 Lung Segmentation in Pulmonary CT images

In CT images, air will appear with a mean intensity of approximately -1000 Hounsfield units (HU), most lung tissue will be in the range of -910 HU to -500 HU, while the chest wall, blood, and bone will be higher (well above -500 HU) [47]. Histogram of a thorax CT image is shown in figure 4.6. Each pulmonary CT pixel can in general be generally divided into 2 major types of voxels[1], 1) voxels within the body soft tissues including the chest wall structures, vessels, muscles and 2) low-density voxels in the lungs, the airway tree or outside the body. Because of significant differences in intensity between the soft tissues and air trapped inside the lung, the lung border is considered as high inflection points of the image; hence applying the wavelet transformation is described in section 4.2 will point out these singularities in the images.

Image intensities vary in different studies due to inconsistency in the dose of radiation or variation in imaging devices. Therefore, each image is enhanced to purge these variations between different images acquired in different studies. In addition, a global transformation, shown in figure 4.4 is applied to each image pixel values in order to not only increase the contrast difference between body and lung, but also between the body tissue and the connective tissue fibers, *interstitum*, that is attached to the lung border or diaphragm; to introduce higher singularity on the edges of interest. This transformation decreases the wavelet edge detection sensitivity in the areas outside of the lung, so those artifacts related to contrast difference between the body objects are eliminated and no post-processing step is required to distinguish between the lung edges and other discontinuities inside the body voxels. Moreover pixel values higher than average body pixels were trimmed to avoid detection of discontinuities between the bones, which are dense structures represented by average intensity of 1000HU, and other soft tissues. After above mentioned enhancements the image is transformed into the wavelet domain, as illustrated in figure 4.8.

[1] A voxel is a unit of graphic information that defines a point in three-dimensional space.

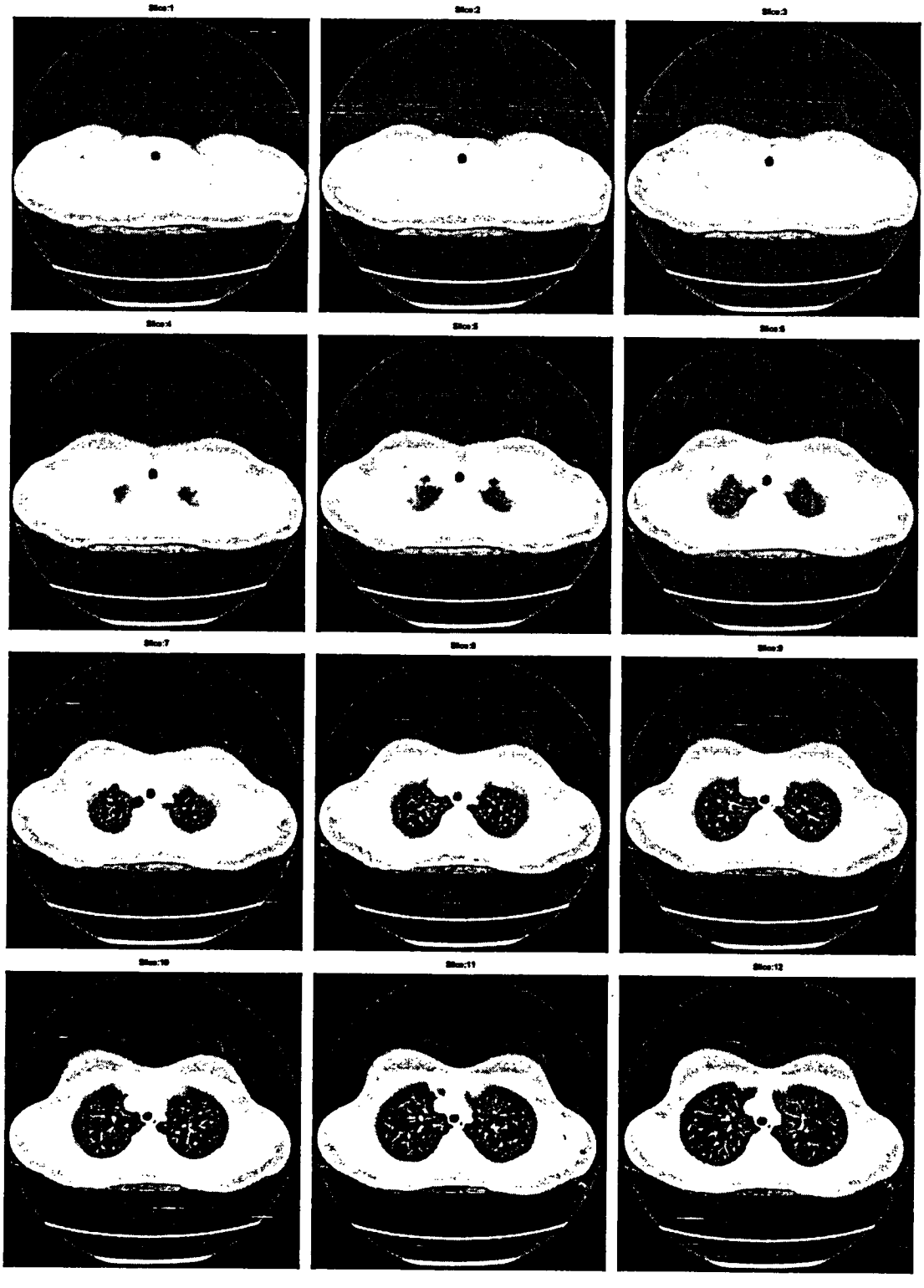

Figure 4.4: Original CT study.

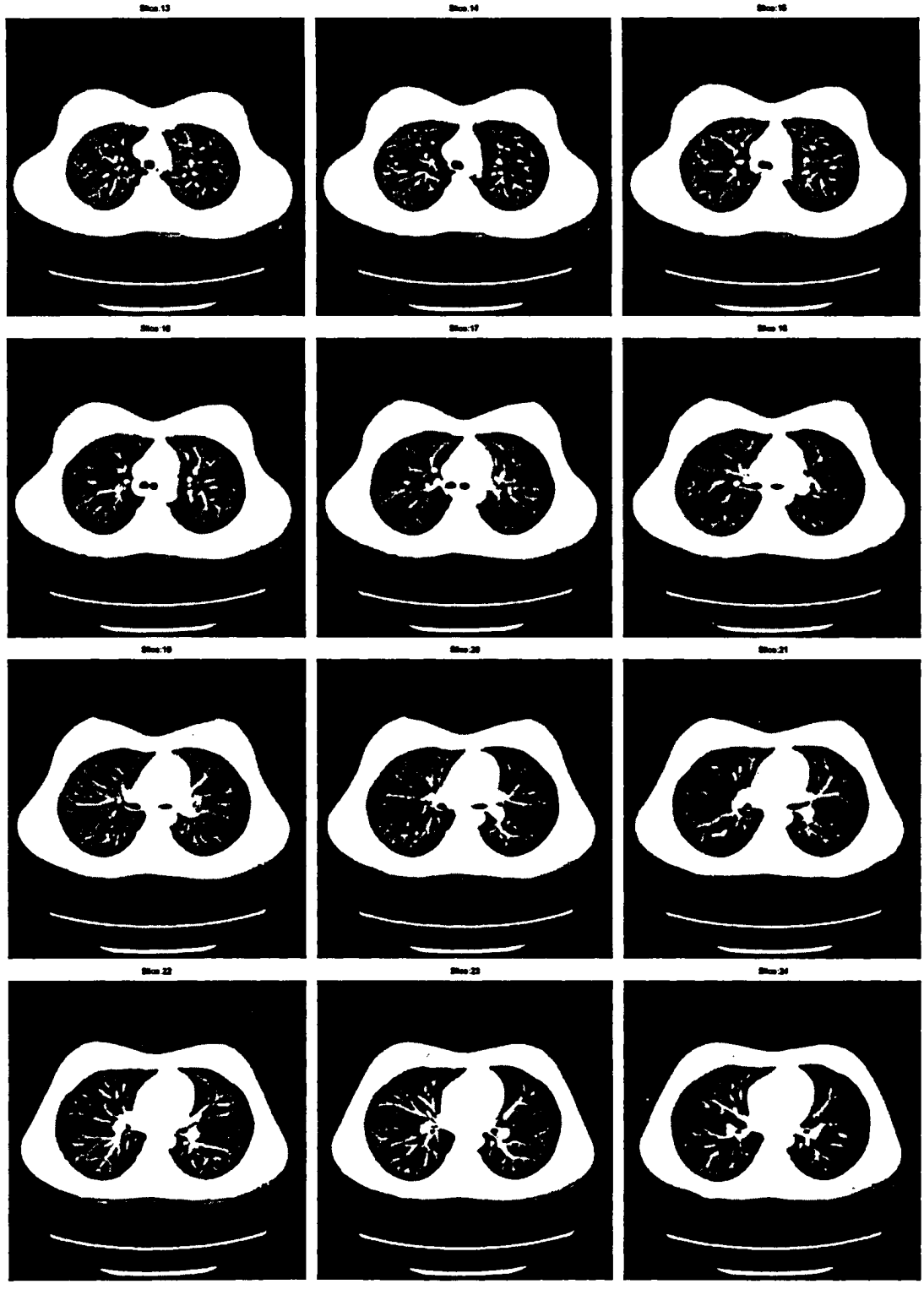

Figure 4.4: Original CT study. (cont)

Figure 4.4: Original CT study. (cont)

Once the mask is obtained using the method described above, lungs are extracted in each CT image. One of the advantages of proposed method is that each CT image can be processed independently of the other images in the studies. This illustrates great advantages of the proposed method. One of these advantages is that the error in segmentation of one slice would not propagate to any other processed slices. The error propagation is the common disadvantage of other methods including region growing and active contours in which the initial seed points or contour of evolution has to be chosen from the previously processed image. However, proposed method could proceed further after the segmentation process in 3D space in order to generate continuously smooth borders. This process potentially can point out attached nodules to the lung wall as will be described later on. A selected series of CT images taken from a patient along with corresponding segmentation results are illustrated in figures 4.9 and 4.10.

The second advantage of processing each image individually is that a particular number of images can be processed regardless of other consecutive images and the number of taken images in the study. This not only provides flexibility to process each individual image but also outperforms the other dependence method in the processing speed. Each study can generate hundreds of images from the pulmonary region when the slice thickness in the acquired series becomes small; hence a enormous number of images may require to be

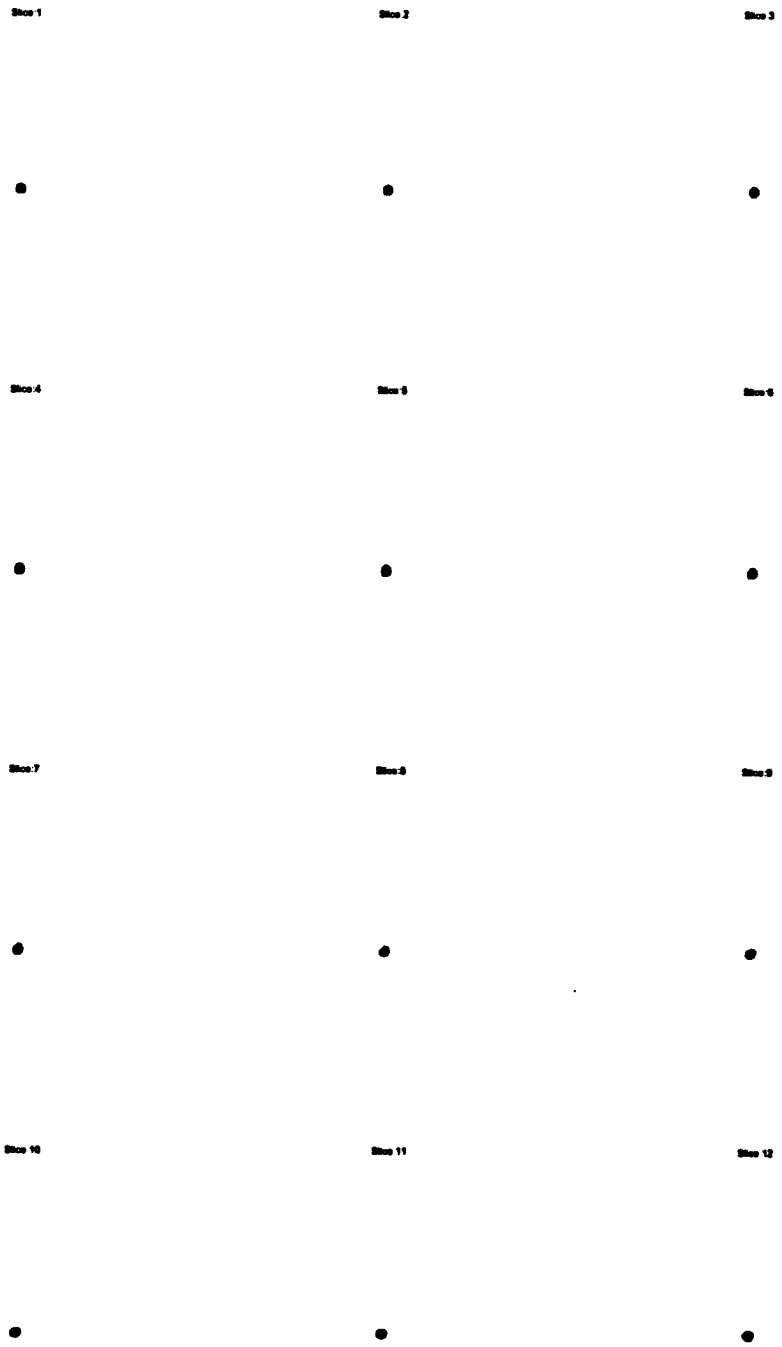

Figure 4.5: Extracted bronchi tree in a CT study.

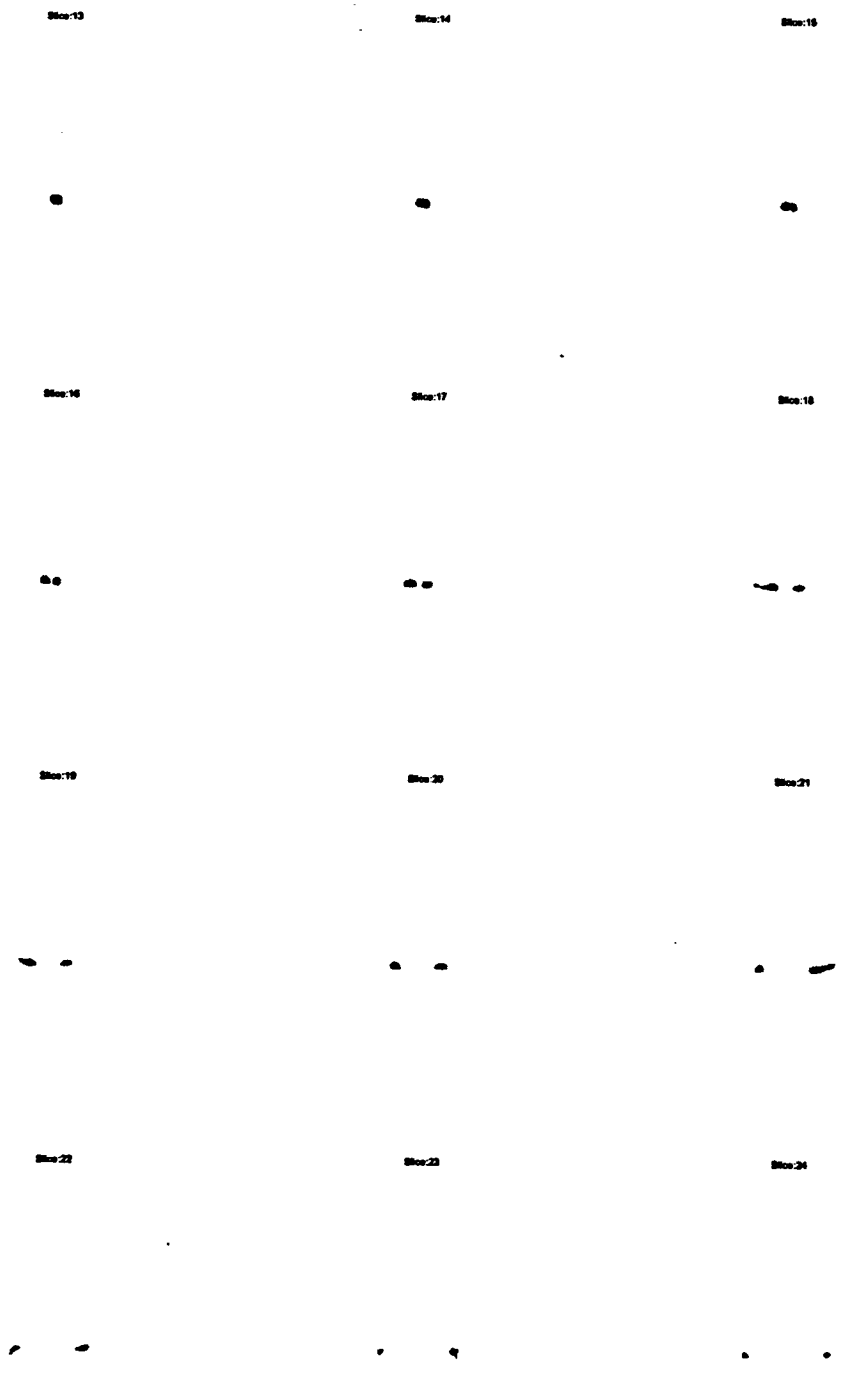

Figure 4.5: Extracted bronchi tree in a CT study. (cont)

Figure 4.5: Extracted bronchi tree in a CT study. (cont)

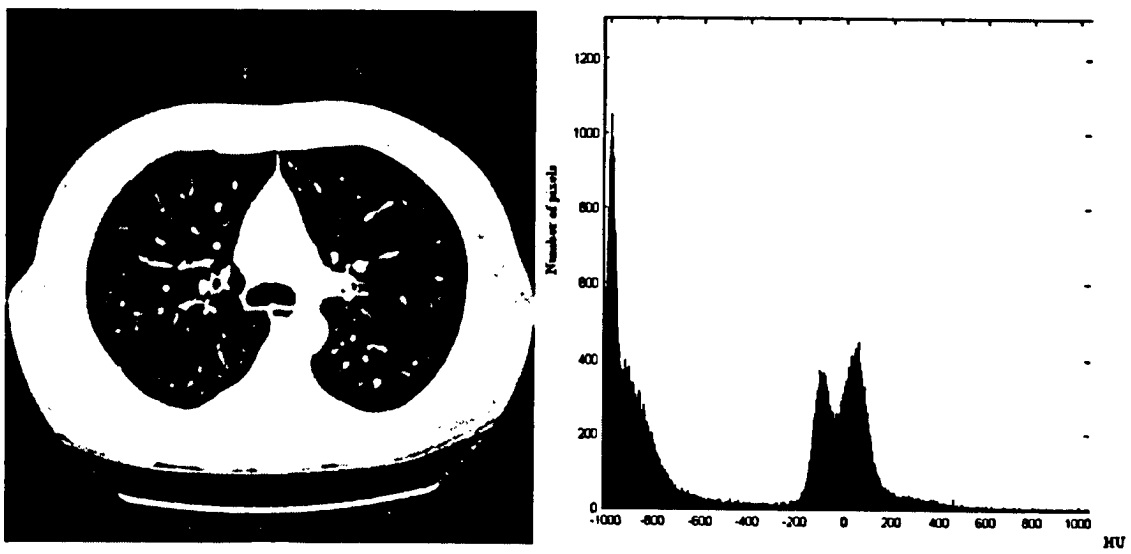


Figure 4.6: Original thoracic CT image and its histogram.

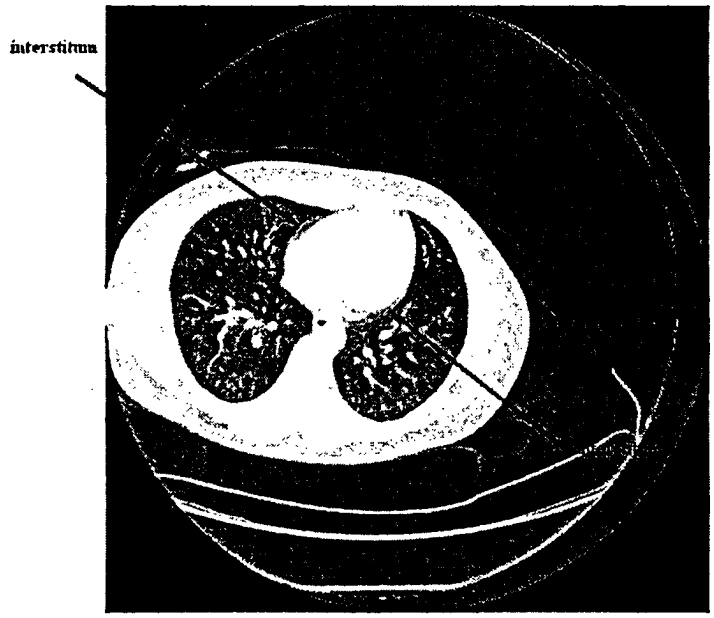


(a)

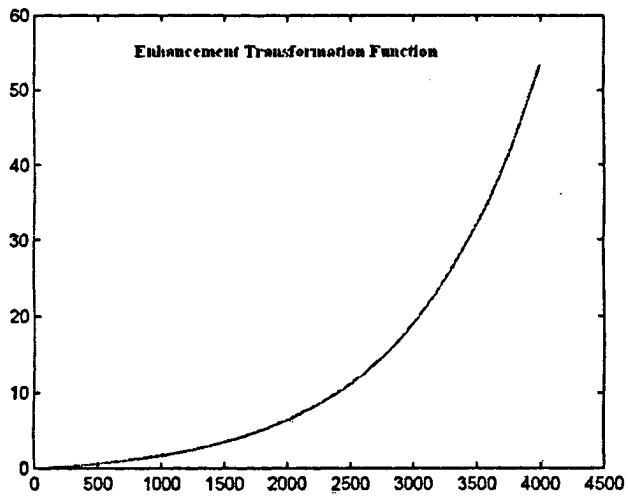


(b)

**Figure 4.7:** (a) Original thoracic image that interstitum pointed on with an arrow (b)transformation function for enhancing the contrast between interstitum and actual lung borders.

processed prior to processing of the slices taken from region of interest. For example an experiment showed that for processing the 48th slice in a series of images a region growing method necessitates 112 seconds whereas the proposed method extracts the lung in about 107 seconds on a computer with 1.73GHz L2 processor and 512MB RAM. After segmenting the lung in the pulmonary images, the extracted regions could be passed to the next processing stage depending on the application that the CAD system has been inclined to be developed for.

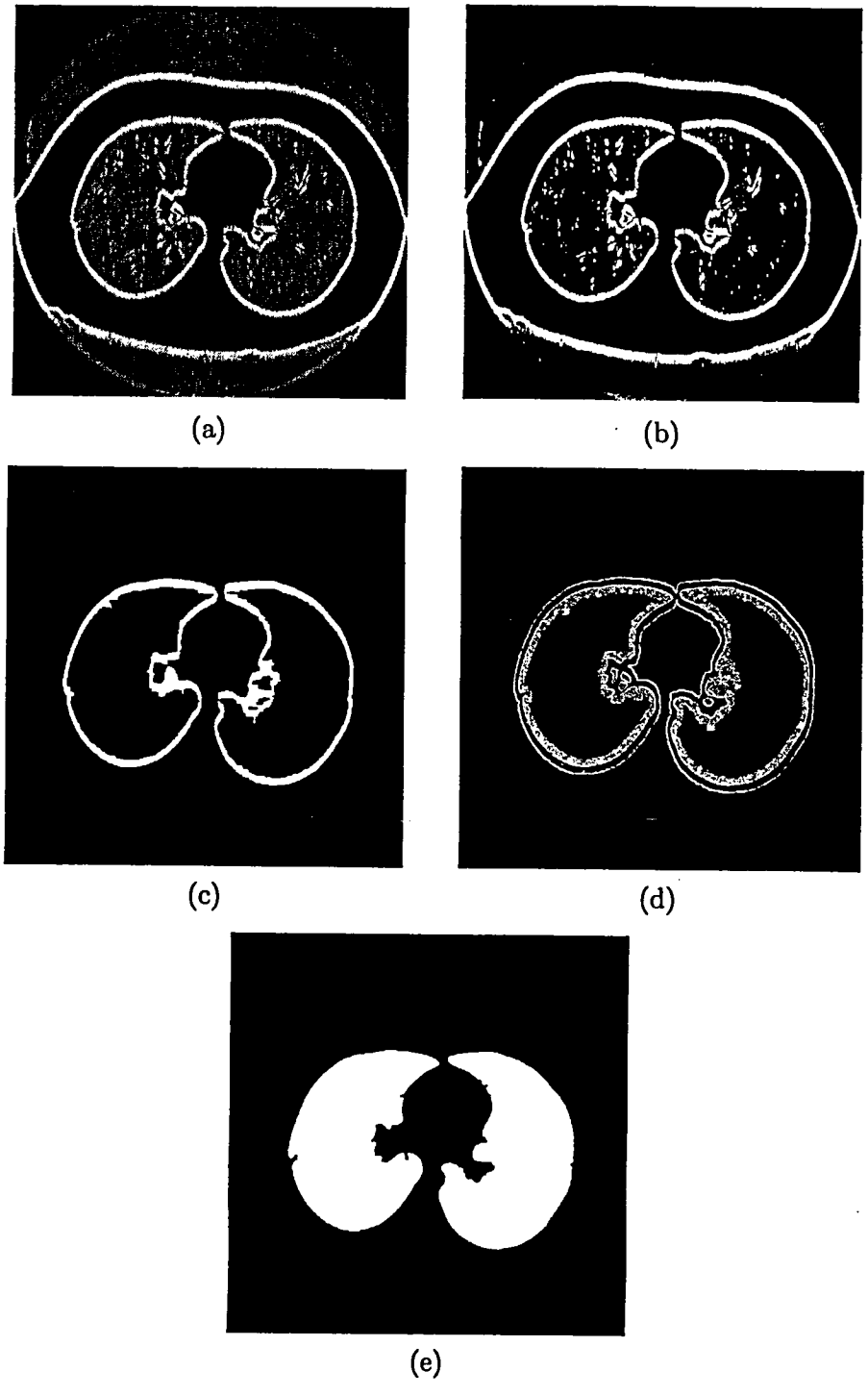


**Figure 4.8:** (a) 2D wavelet transformation, shows the high scales (b) edge map image (c) obtained edge mask from high scales. (d) wavelet transformation in the first scale (e) Final mask.

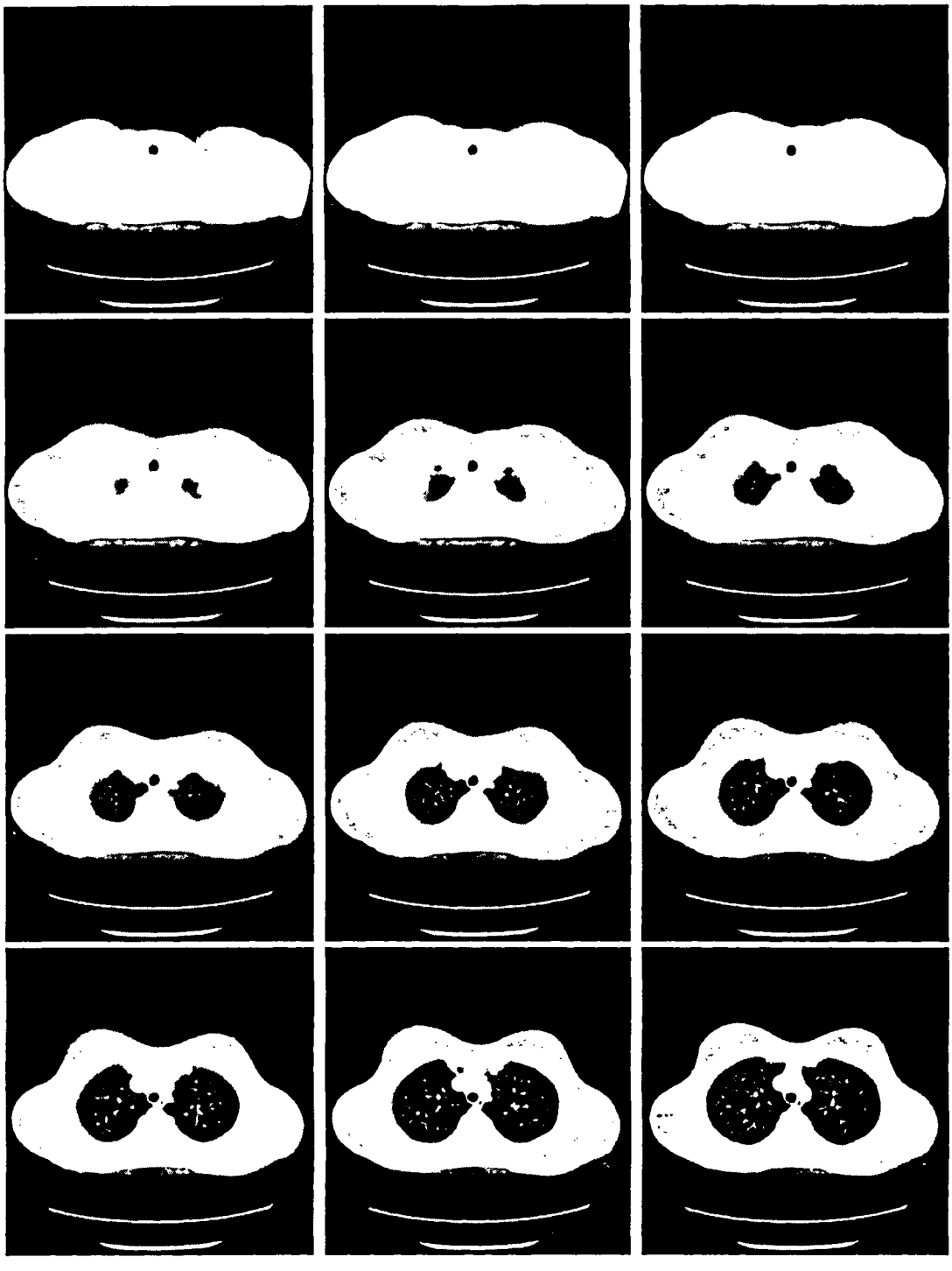

**Figure 4.9:** A series of DICOM CT images from one patient.

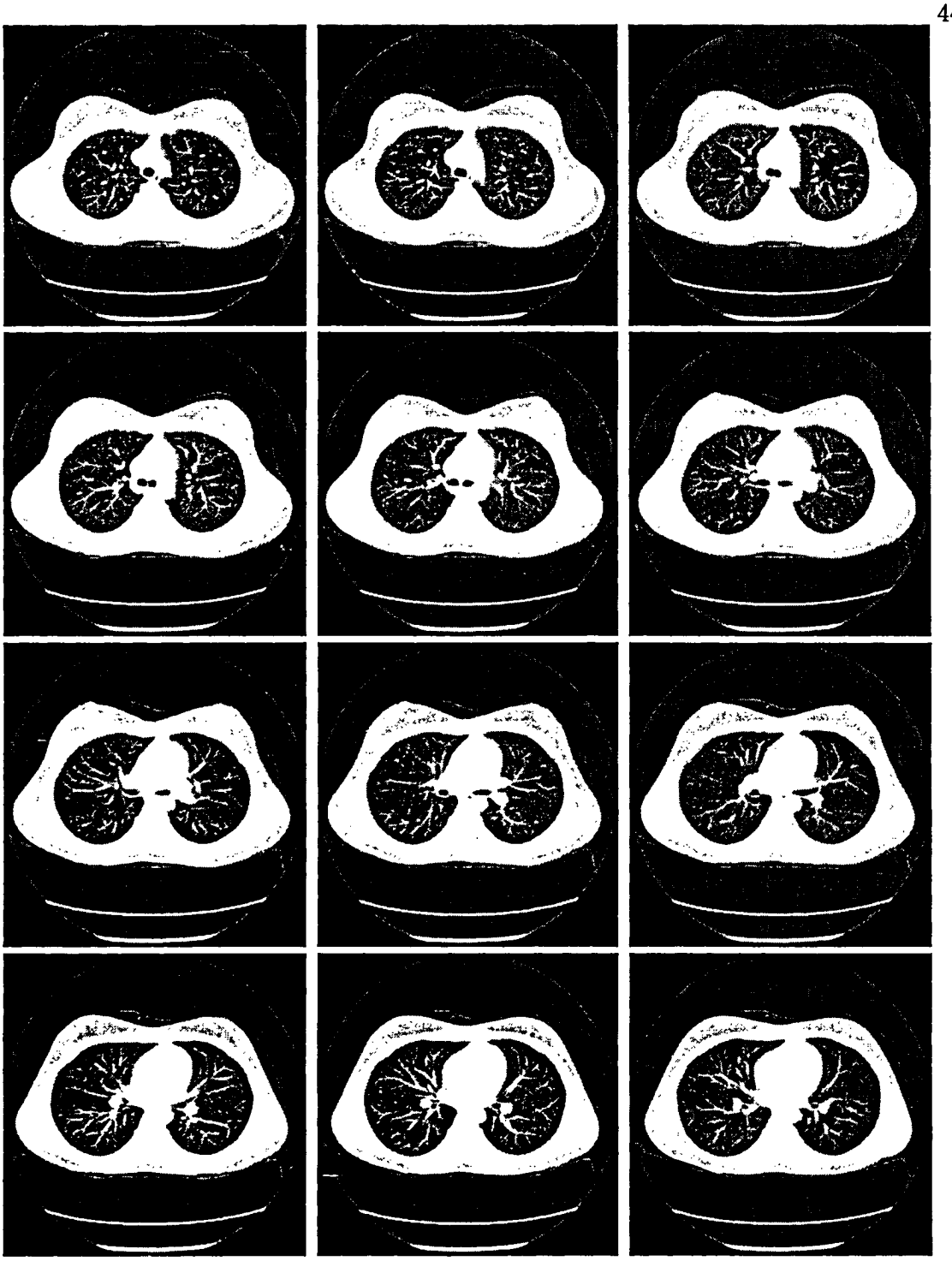

Figure 4.9: A series of DICOM CT images from one patient. (cont)

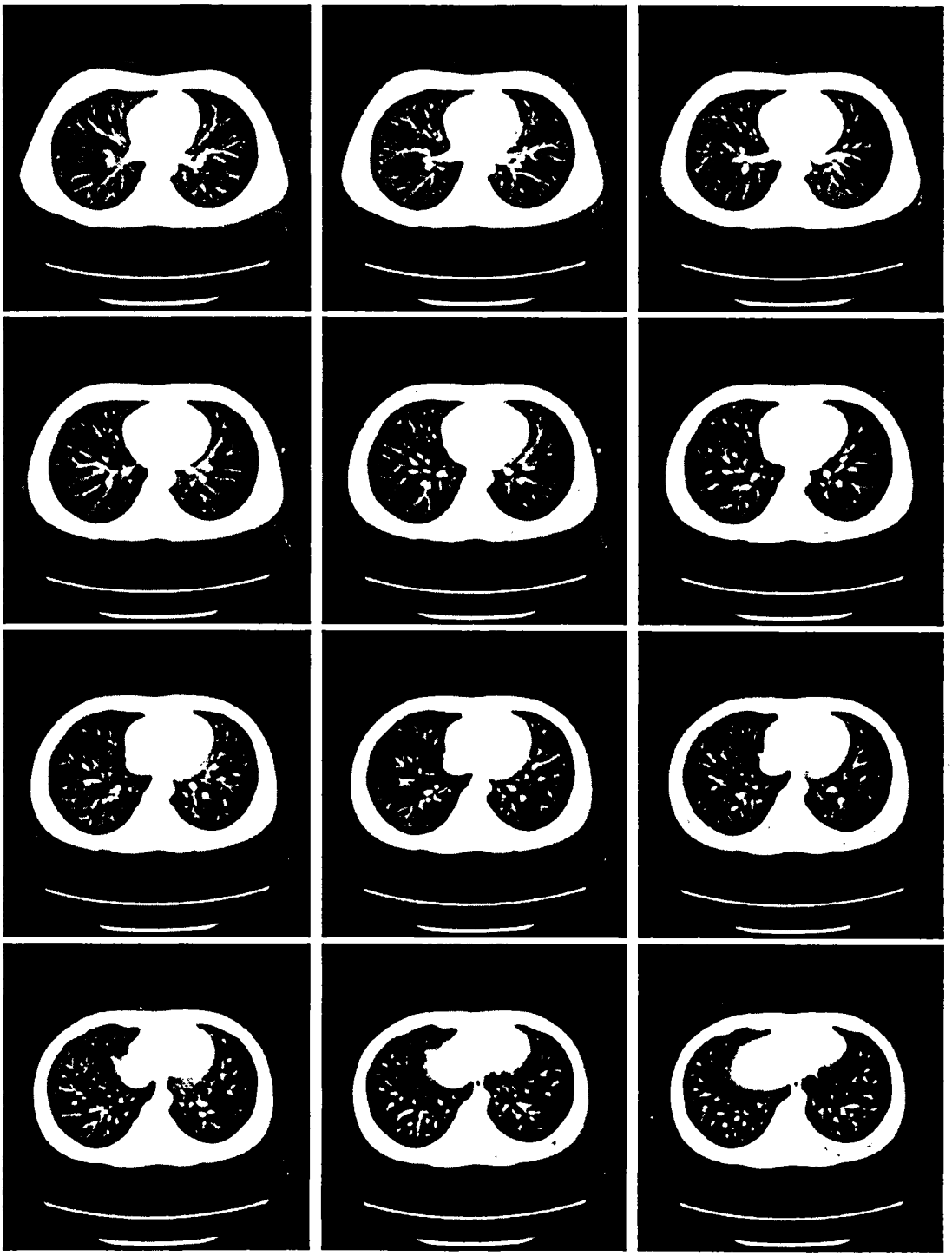

Figure 4.9: A series of DICOM CT images from one patient. (cont)

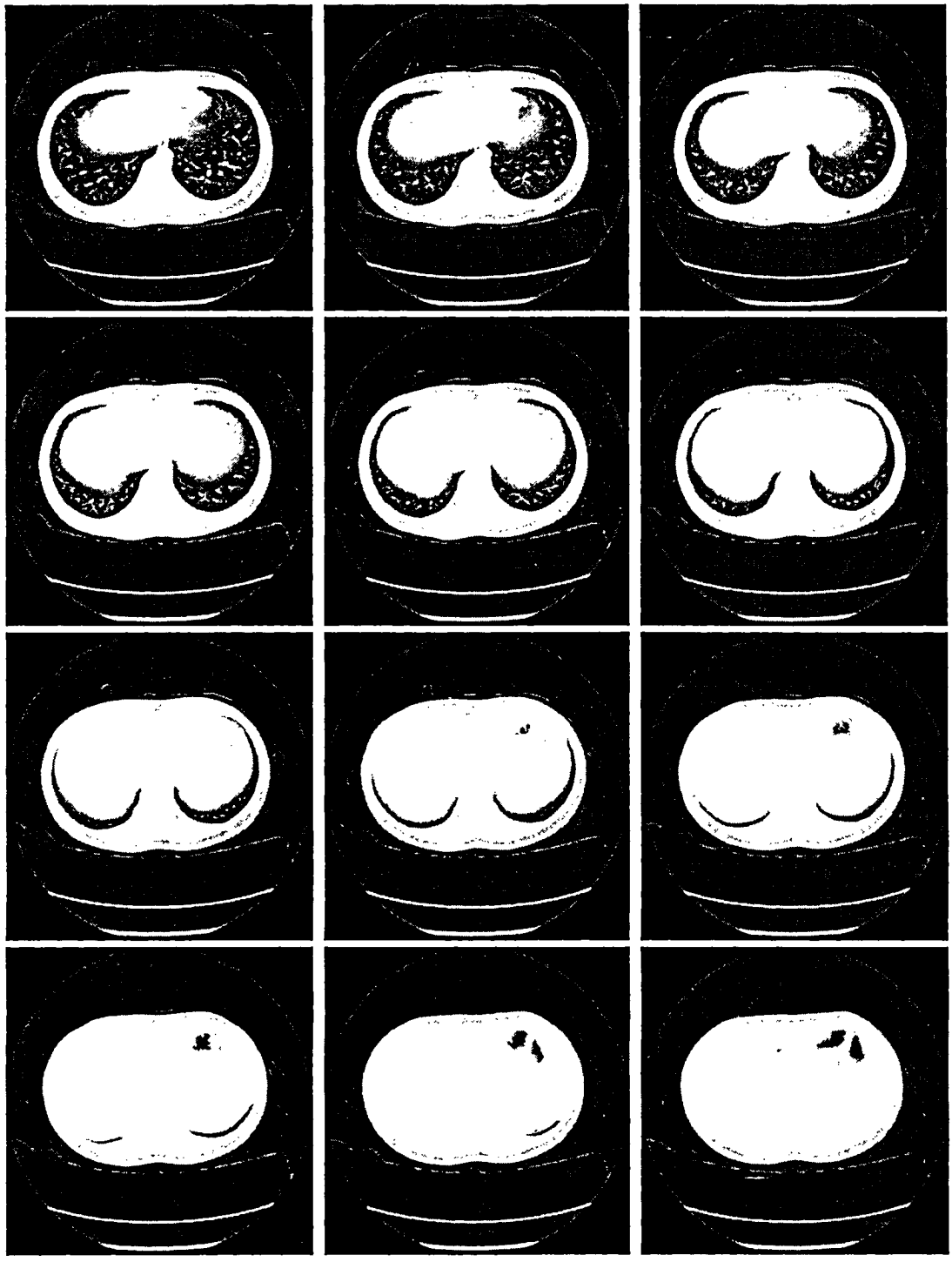

Figure 4.9: A series of DICOM CT images from one patient. (cont)

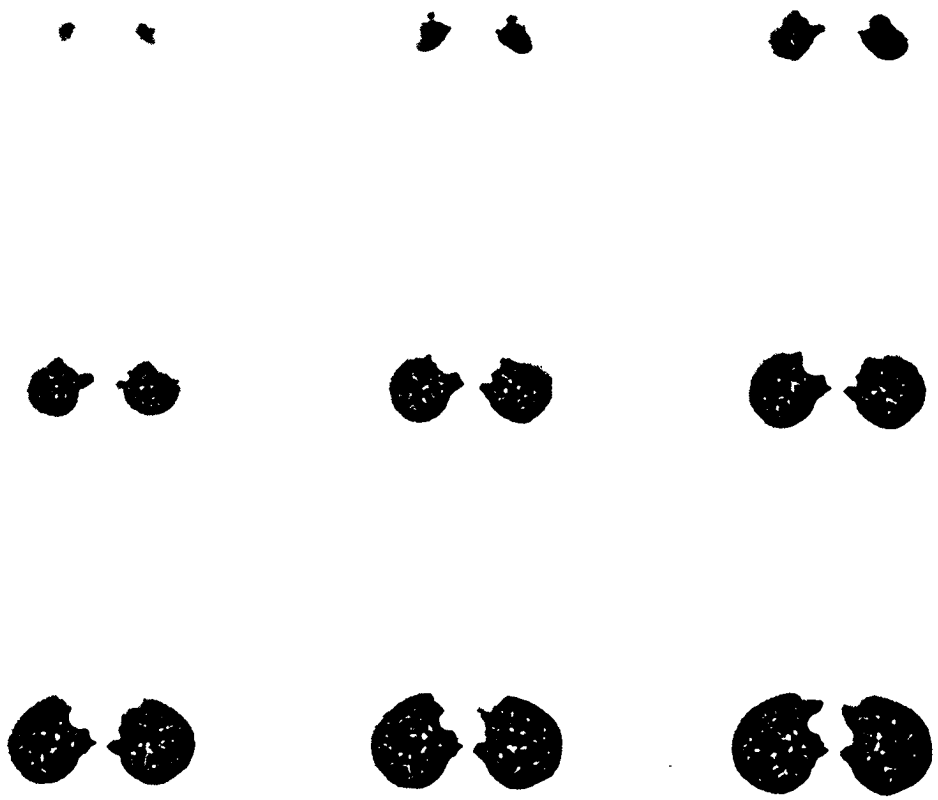

Figure 4.10: Extracted lung from the series of DICOM CT images illustrated in figure 4.9. Black blocks represent that nothing was extracted as lung.

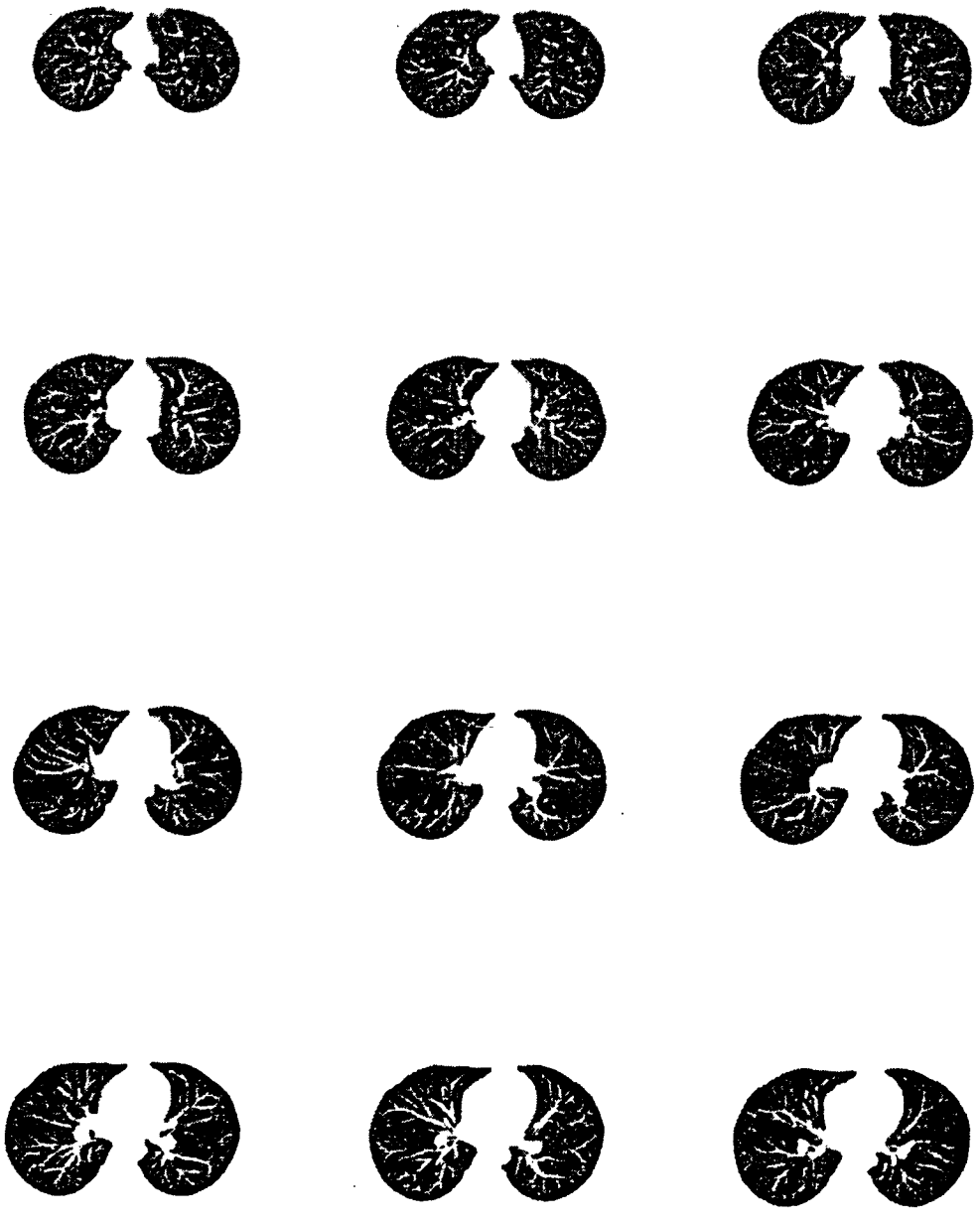

Figure 4.10: Extracted lung from the series of DICOM CT images illustrated in figure 4.9. Black blocks represent that nothing was extracted as lung. (cont)

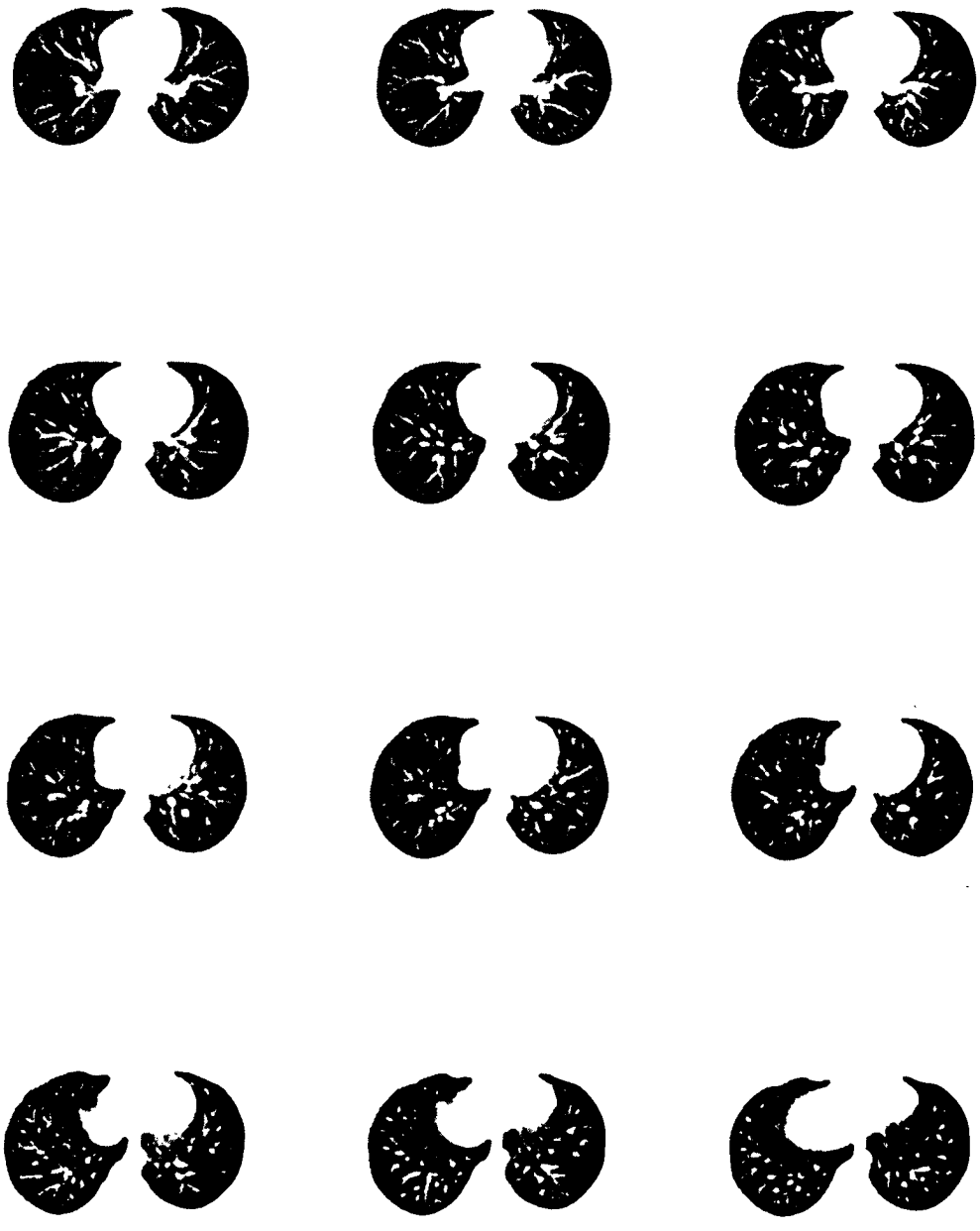

**Figure 4.10:** Extracted lung from the series of DICOM CT images illustrated in figure 4.9. Black blocks represent that nothing was extracted as lung. (cont)

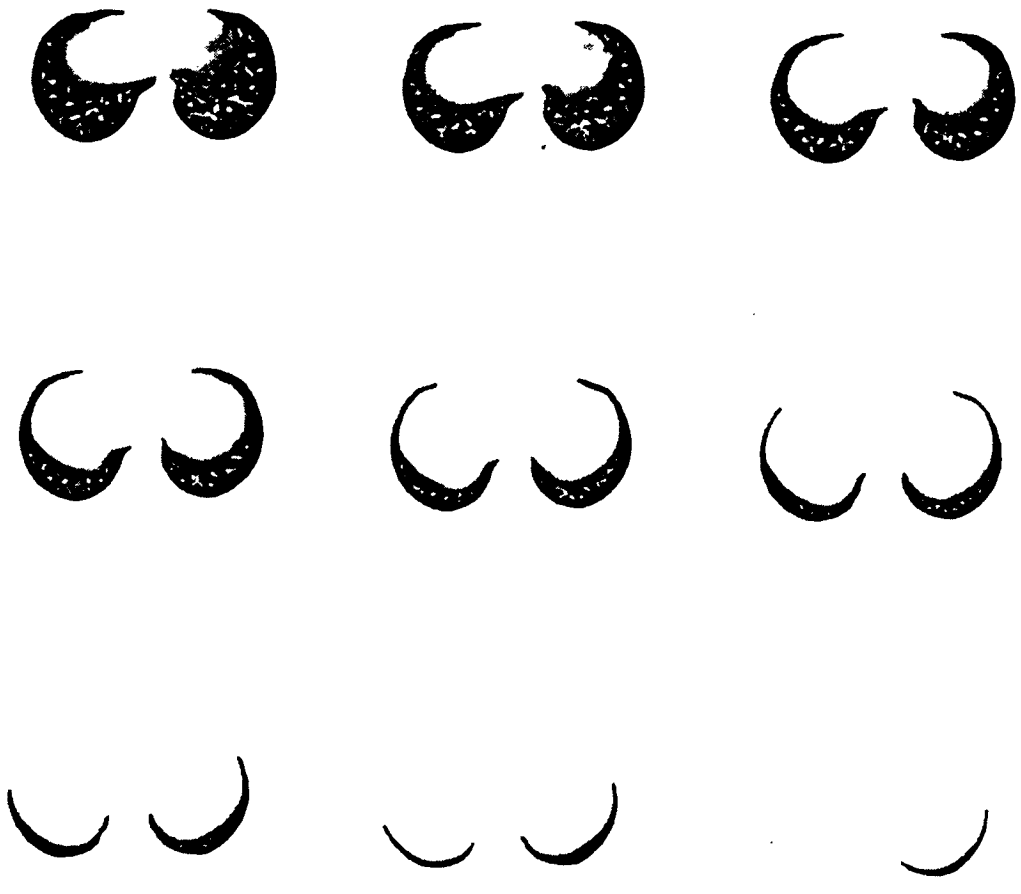

**Figure 4.10:** Extracted lung from the series of DICOM CT images illustrated in figure 4.9. Black blocks represent that nothing was extracted as lung. (cont)

## 4.5 Selective Enhancement Filter for Nodules

Vessels, airways, aerated lung and possibly abnormalities can be found inside the lung in each pulmonary CT image. Among those, airways and aerated lung appear as dark objects whereas vessels and other focal abnormalities including nodules are seen as a bright object due to their X-ray attenuation level. Therefore, low intensity pixels can be eliminated when there is a problem of nodule detection. Thresholding may be considered to segment the nodule in the images but thresholding of the original CT images may confront to the following issues:

1. Some nodules have very low HU and low contrast which makes the proper selection of the threshold value very difficult. Eventually choosing a low threshold value dramatically increases the false positives.

2. Many nodules have intensities similar to those of the vessels and bronchia walls which bring difficulties into the picture during the extraction of nodules with low false positives.

3. Juxta-vascular and pleural nodules are required to be detached from the connected normal anatomical structure.

Vessels and nodules usually appear with quite the same intensity ($\sim$ 0HU) in the CT images. Despite holding the similar intensity, vessels are formed as tubular structures while nodules are shaped as spherical structures, except for pleural nodules. Extraction of spherical structures within the images reduces the number of false positives substantially; hence utilization of a 3-D enhancement filter which ignores tubular structures while enhancing spherical ones is considered as a pre-processing step to the nodule classifier module.

A selective enhancement filter sensitive to the shape and intensity is proposed as a pre-processing step and as one of the inputs to the nodule classifier. This filter is based on eigenvalues of matrices formed from wavelet transformations of the pulmonary CT images.

A typical well-circumscribed nodule profile is illustrated in figure 4.11. This profile can

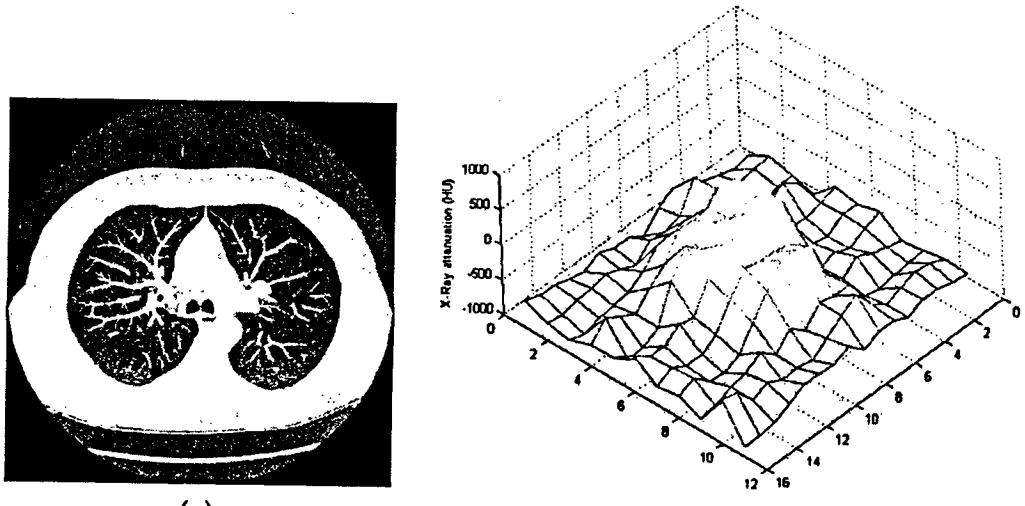


(a) (b)

**Figure 4.11:** (a) 3D rendered thoracic CT image. (b) 2-D profile of the nodule in the left lung lube.

be accurately approximated by a discrete Gaussian shape function [30, 31]. It is known that the wavelet transformation would provide its best performance if the mother wavelet is defined as similar as possible to the information of interest in the image; hence spline and its derivatives are chosen as wavelet bases of employed wavelet transformations. Upon applying derivative of spline function (figure 4.12) to an image, smoothed derivatives of the original image are determined, equation (4.4).

Lung nodules are usually denser at the center so their 2D X-ray attenuation, HU, profile at each axial slice has a maxima around the center and then gradually decreases upon reaching the borders. Due to this well-defined characteristic, nodules are considered as Gaussian shaped structures in many studies [30, 29, 63, 64]. Lung nodules smaller than 1cm are the spotlight of this thesis. These types of nodules occupy a few pixels within each slice so their intensity profile can be approximated by a Gaussian function. The pulmonary nodules, except for pleural nodules, are assumed to be defined as Gaussian shaped structures in order to design the enhancement filter. Assuming that the intensity of a nodule is defined as

$$f(x,y,z) = exp(-\frac{x^2+y^2+z^2}{2\sigma^2}) \tag{4.8}$$

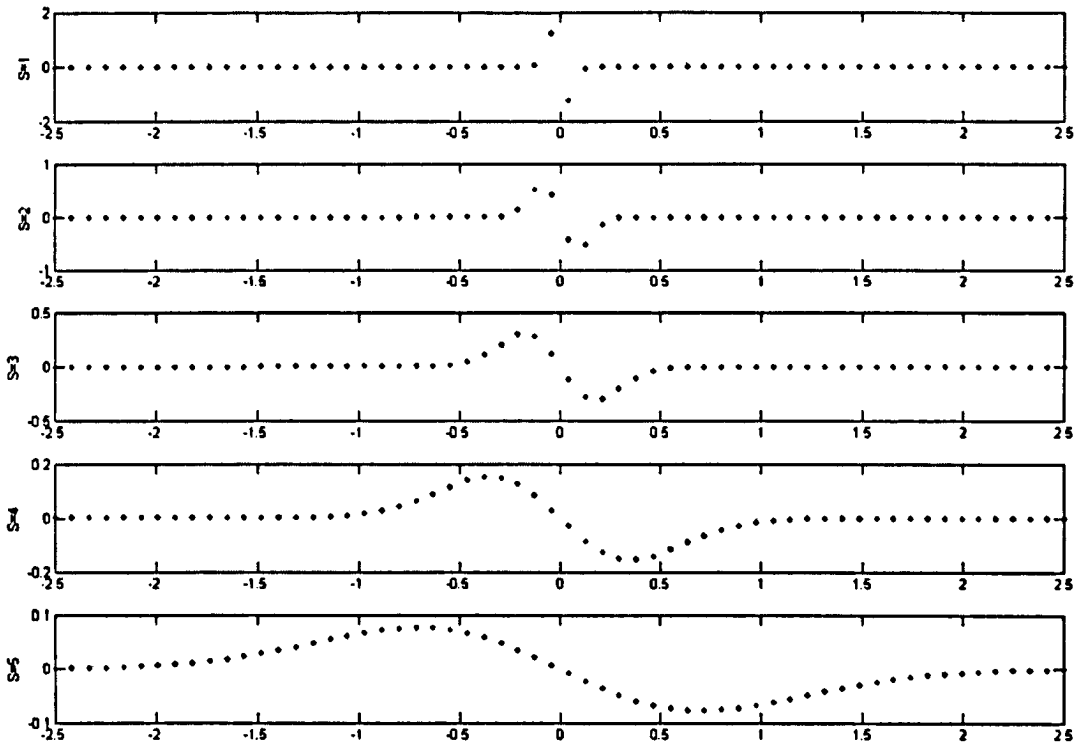

**Figure 4.12:** Wavelet transformation function over each scale.

Where $\sigma$ represents the scale of the nodule. Hessian matrix corresponding to each voxel over the thoracic series of images is defined as

$$H = \begin{bmatrix} f_{xx} & f_{xy} & f_{xz} \\ f_{yx} & f_{yy} & f_{yz} \\ f_{zx} & f_{zy} & f_{zz} \end{bmatrix} \tag{4.9}$$

Where $f_{ab} = \frac{\partial^2}{\partial a \partial b} f$. For this idealized shaped nodule defined by equation 4.8, all six mixed second derivatives $f_{xy}, f_{xy}, f_{xz}, f_{yz}, f_{xz}$, and $f_{yx}$ are zero in the center while $f_{xx}, f_{yy}$, and $f_{zz}$ are equal to $-\frac{1}{\sigma^2}$. Therefore, eigenvalues of the hessian matrix ($\lambda_1$, $\lambda_2$, and $\lambda_3$) are equal to $-\frac{1}{\sigma^2}$. Suppose eigenvalues are indexed such that $|\lambda_1| \geq |\lambda_2| \geq |\lambda_3|$.

$L = \frac{|\lambda_3|}{|\lambda_1|}$ is considered as likelihood ratio of existence of a spherical object over a linear/tubular structure. $L$ assigns a value of 1 to a spherical object, defined in equation 4.8, while offering a lower value to other possible objects. For example $L$ offer a value close to zero to a tubular structures since $\lambda_3$, minimum directional second derivative value, is very

close to zero for this class of objects. The simple likelihood ratio between eigenvalues does not provide high level of specificity. A reason for this is that the filter is completely sensitive to the basis function wavelets and also small eigenvalues produced by an arbitrary object can still lead to a significant response. Therefore, the likelihood ratio is multiplied by a function, $M$, more sensitive to the pixel intensity to overcome lack of adequate discriminatory power for distinguishing nodules from other objects. To determine this function, it should be considered that magnitude of $\lambda_3$ is receiving high attention in this manner since its magnitude automatically indicates existence of a bright object in a dark background as of a nodule. Moreover $M$ should provide relatively much higher response to a spherical shaped rather than tubular shape objects in the images. This brings a better separation between vessels and nodules. One of the simplest and suitable functions for this manner is $M = \lambda_3^2$. Since nodules are bright objects in the dark background, it should be also brought to the consideration that the eigenvalues of $H$ are negative numbers. Consequently the filter output is defined as:

$$EF(x,y,z) = \frac{|\lambda_3|^3}{|\lambda_1|} .\sigma_o^4 \qquad \lambda_3, \lambda_2, \lambda_1 < 0 \tag{4.10}$$

Where $\sigma_o$ is scale of the mother wavelets and is multiplied to the function for the normalization purposes. A number of researches have employed enhancement filters mostly to distinguish lines in images [65, 66]. It should be noted that the filters employed in these studies are likely to produce a large response for a nodule-like object whereas the introduced filter has good sense of specificity over picking nodules and rejection of the other objects. Sato *et al.* [67, 68, 69] developed a blob enhancement filter in which a empirically unknown parameter should be determined. Although this parameter brings more flexibility, it may be difficult to make an appropriate choice of this parameter depending on the application. Moreover, theoretically Sato's blob filter will produce the same outputs for these two different objects when the diameter of a circle (nodule-like object) is equal to the long axis of an ellipse regardless of its short axis-elongated (if the short axis is small).

The proposed filter potentially suffers from lack of accuracy due to anisotropic voxels in 3D CT images. The enhancement filter is known to provide the highest level of enhancement

performance for 3D images with isotropic voxels (uniform voxel spacing). Two solution come to the picture at this point. 1) Trilinear, sinc or B-spline interpolation technique can be employed to make the voxel size equal in the all three dimensions. Interpolation is not only computational expensive but also can potentially affect the filter's response. 2) It is also possible to construct enhancement filters that can be applied directly to images with anisotropic voxels without explicit interpolation. This type of filters are highly dependent on the voxel spacing and should be adjusted upon changing the voxel size in each dimension.

To reduce the computational expense and complexity and to avoid insertion of any additional information to the series of images, combination of some consecutive slices with a simple technique, known as Maximum Intensity Projection (MIP), is employed. Basically MIP utilizes the maximum function to generate a 2D image from a number of CT slices. The CT slices within $5mm$ axial distance of the slice of interest are combined to generate the MIP image. An example of MIP image is shown in figure 4.13. It has been proven that support vector machines are capable of extracting the lung nodules in the image produced by this technique.

The introduced enhancement filter can be modified for a 2D image in order to detect a circle in a 2D image as follows. In maximum intensity projection image a nodule is presented as a circle defined by a gaussian function as shown below

$$f(x,y,z) = exp(-\frac{x^2+y^2}{2\sigma^2}) \tag{4.11}$$

Where $\sigma$ represents the scale of the nodule. Because of the similarity between 2D and 3D cases, the 2D enhancement filter is introduced based on the 3D filter formulation by modifying equations 4.9 and 4.10:

$$H = \begin{bmatrix} f_{xx} & f_{xy} \\ f_{yx} & f_{yy} \end{bmatrix} \tag{4.12}$$

$$EF(x,y,z) = \frac{|\lambda_2|^3}{|\lambda_1|}.\sigma_o^4 \qquad \lambda_2, \lambda_1 < 0 \tag{4.13}$$

It should be noted that what has been discussed for a 3D enhancement filter applies to the above-defined 2D filter also. Output of this filter is shown in figure 4.14 as an example of its performance.

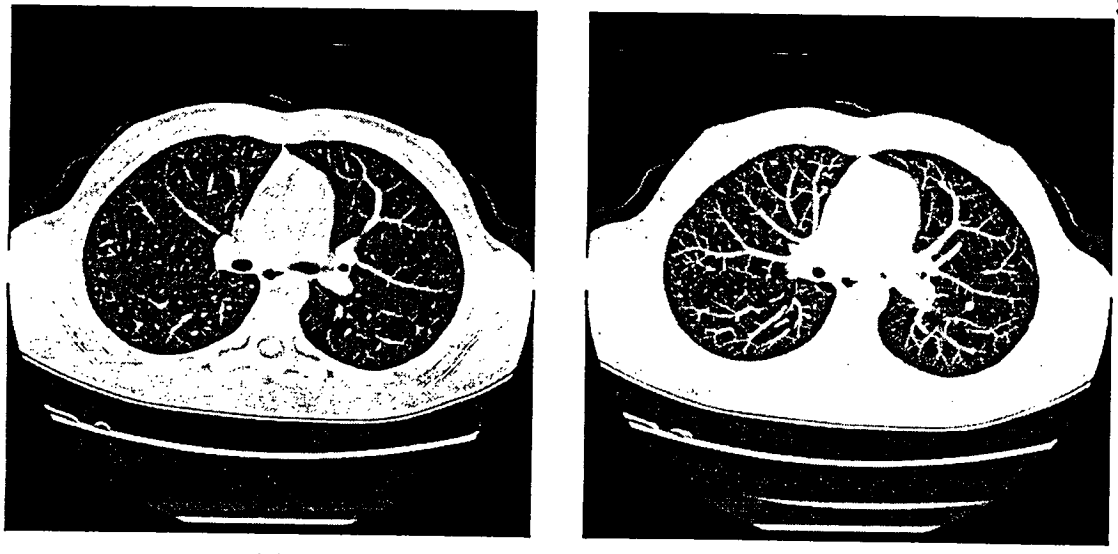

(a) (b)

Figure 4.13: (a) Original thoracic CT image (b) corresponding maximum intensity projection image.

Output of this filter is presented to the SVM nodule classifier to provide sense of circularity/sphericality to the artificial intelligence detector.

This system considers the circularity and the profile of an object in order to classify the certain object as an abnormality or a nodule. Usually pleural nodules are not appear in shape of a circle in the CT images and they are attached to the lung wall; hence the introduced enhancement filter fails to detect those nodules and present them to the SVM classifier. To overcome this issue, another set of data consist of the objects within 1.5cm to the lung border intensity and size is presented to another SVM classifier to detect the pleural nodules. Generally an object bigger than 1cm is a focal abnormality in that area. This system tends to detect nodules close to the lung border since the vessels are branched are much smaller than the nodules in that area. For the juxtapleural nodules, the segmentation mask is smoothed by a rolling ball. The smoothing step causes this type of nodules to be included in the segmentation and gets count as the lung area, so they would be presented to the classifier.

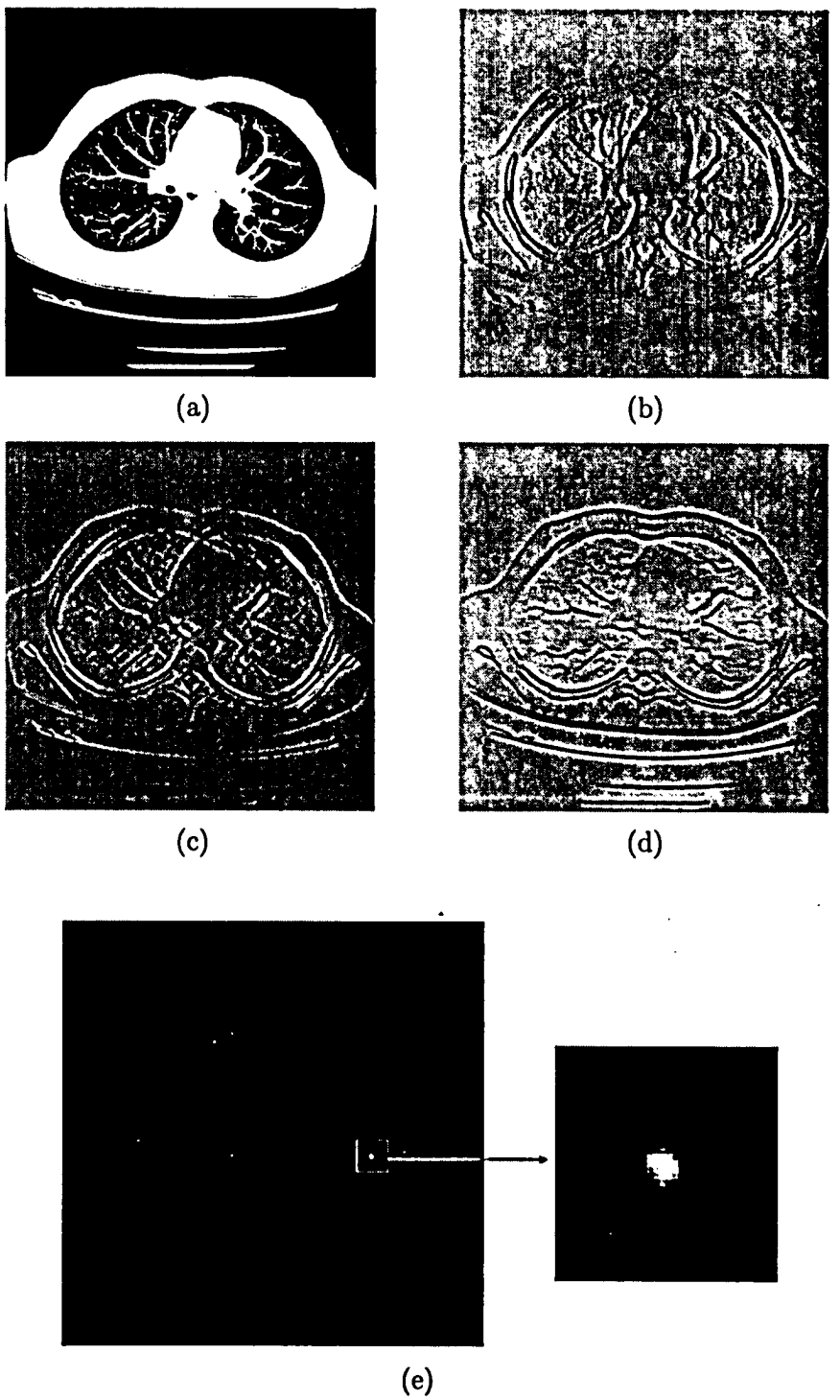


**Figure 4.14:** (a) MIP image chosen arbitrary from a CT study (b) $f_{xx}$ (c) $f_{xy}$ (d) $f_{yy}$. (e) the enhancement filter response.

# Chapter 5

# Experiments

Experimental result of the discussed methodologies through the first four chapters is provided in this section. To present all the acquired results, this chapter is divided into subsections where each subsection corresponds to one of the methodologies discussed in previous chapters.

## 5.1 Nodule Detection

### 5.1.1 Dataset

Not having a unique dataset as a gold standard consists of various pulmonary CT studies is a significant short come to compare the different methods. Sometimes this flaw goes too far to the point that some researchers evaluated the performance of their approaches on a set of synthetic nodules. Although this can be considered as an initial step to design and evaluation of the system, it can never be considered as an assessment on a real CT data. The data acquired from a real subject can be far more challenging for the CAD system. In other words, a CAD system may provide a poor appraise on a real data while it can offer a considerable performance on a synthetic data.

The database composition may have a momentous impact on the system performance. In this research, three different databases are processed to evaluate the system on the CT studies acquired within a spacious variety of nodules in size and distribution.

1. CT studies acquired from child patients with the average age of 12 in The Hospital

for Sick Children, Toronto, Canada. This dataset was reconstructed as slices of 512 by 512 pixels and slice thickness of 5mm. The CT examinations were performed on a GE Medical System CT scanner with a protocol of 120mA to 160mA and 120kVp. Dealing with this dataset presents a challenge due to its slice thickness. Processing of this dataset can be challenging for many nodules detection methodologies due to its large slice thickness (axial resolution). This low axial resolution may lead to the loss of some small nodules by the CAD which are appear in only one slice or may have been left between the slices. Many of the proposed methods got size as a criteria on their decision making process, therefore they can easily miss this kind of nodules. As described earlier, the proposed enhancement filter in this thesis is sensitive to the resolution difference between the dimensions. In this dataset the average resolutions in the X and Y directions are calculated as 0.7mm while the average resolution in the Z direction is 5mm. The proposed CAD tends to provide an acceptable performance in processing of this database even though the axial resolution is about 7 times lower than the other ones.

2. CT studies acquired from child patients with the average age of 10 in The Hospital for Sick Children, Toronto, Canada. The CT examinations were performed on a GE Medical System CT scanner with a protocol of 120mA and 120kVp.This dataset was reconstructed as slices of 512 by 512 pixels and slice thickness of 2.5mm.

3. A database is endowed by collaboration of International Early Lung Cancer Action and Cornell University research groups to be used for the performance evaluation of different computer aided detection systems. The database consists of an image set of low-dose documented whole-lung CT scans. The CT scans were obtained in a single breath hold with a 1.25mm slice thickness. Each study in this study contains over 200 pulmonary CT images.

It should be advised that these databases contain a broad assortment of nodules of different sizes and types. The tiny nodules smaller than the area of a 2mm circle are discarded

| Patients | slice thickness | Average number of slices | Sensitivity | TNs/case | FPs/case |
|---|---|---|---|---|---|
| Children | 5mm | 50 | 88% | 1 | 6 |
| Children | 2.5mm | 62 | 87% | 1.1 | 7 |
| Adult | 1.25mm | 230 | 85% | 0.8 | 3 |

**Table 5.1:** Performance of the proposed methodology on the databases.

since they are not the scope of this thesis while area of 3mm circle or larger is considered as the minimum nodule size criterion by some researches [14, 17, 34, 70, 71, 3].

To appraise the performance of the proposed method performance on extraction of pulmonary lung nodules in the CT images, 12 patients from each database are presented to the trained system. For each database the system is trained from a patient (13 nodules on average) and 2 healthy slices. Table 5.1 reveals the obtained performance of the proposed method for each database. The result came out as 6FPs, 1 True Negative (TN) per case (average of 50 slices per study) on the database taken from children with 5mm slice thickness; 7FPs, 1TN per case (average of 62 slices per study) on the database taken from children with 2.5mm slice thickness; and 3FPs, 0.8TN per case (average of 230 slices per study) on the database taken from adults with 1.25mm slice thickness.

Some of above mentioned FPs are nodules with size between 2mm and 3mm circles (usually about 4mm in diameter) or the vessels moving in axial direction for more than 6mm. Tiny nodules are usually seen with low intensity in the images due to partial volume effect of the scanners. The CAD system missed this type of nodules mostly due to its low intensity profile. An example of this nodule is illustrated in figure 5.1.

The obtained results are compared with previously reported studies by Computer Vision and Image Processing group of Ryerson University [72, 73] as of table 5.2. The comparison has been done by these two studies since all these studies have processed a common dataset, the dataset with 5mm slice thickness.

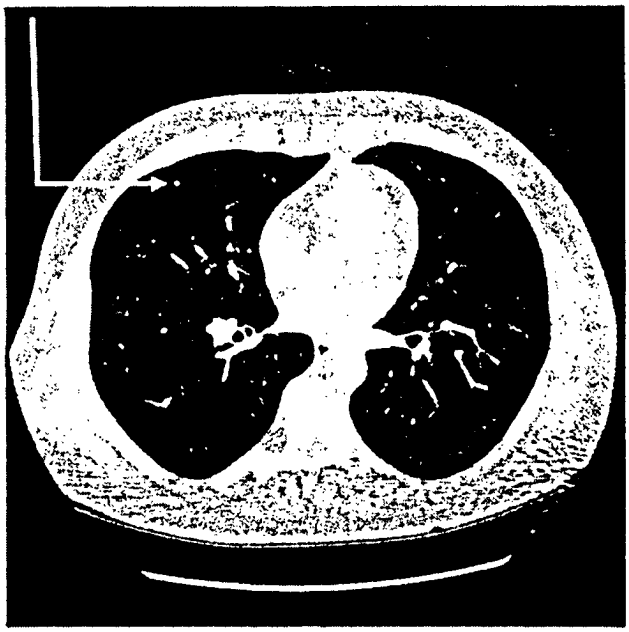

**Figure 5.1:** A tiny nodule, pointed by an arrow, on the interior part of the right lung.

| Researcher | Sensitivity | FP/case |
|---|---|---|
| Dajnowiec | 71% | 160 |
| Memarian | 72% | 120 |
| Current research | 85% | 6 |

**Table 5.2:** Comparison of performance results with previous works.

## 5.2 Segmentation Results

There was a very close correlation between the actual lung borders and automatically identified borders by computer. Moreover, comparison between the segmentation results and manual segmentation of an experienced radiologist, showed that the proposed algorithm is capable of segmenting lung in pulmonary CT images within high accuracy. The borders were matched except in the cases where the lung border had fuzzy edges; even in these cases the difference was less than 3 pixels. The algorithm may prove its advantage in applications where the number of images to be processed is high and processing time is important because of its computational inexpensive nature in comparison to other existing segmentation methods. This method does not involve any iterative steps unlike other methods such as

| Methodology | Wavelet | 3D region growing | Watershed |
|---|---|---|---|
| Process time | 107Sec | 112Sec | 144Sec |
| Accuracy ranking | 1 | 3 | 2 |

**Table 5.3:** Comparison between wavelet, watershed and 3D region growing based methods in terms of their segmentation speed and accuracy for one patient and the series shown in figure 4.9.

snakes, or traditional watershed transform. Results obtained from these methods have to be modified after each iteration till they meet their termination criteria(s). A comparison between 3D region growing [74], marker-based watershed [75], and our proposed method in terms of speed and accuracy (comparison between the segmentation results and radiologists' manual segmentation) is illustrated in table 5.3 for one patient and the series shown in figure 4.9. It should be noted that the processing times has been calculated upon running MATLAB software on a computer with 1.7GHz processing speed with 512MB RAM. For further computation cost reduction, the transformation can be computed with lower computation order upon the numerical implementation of fast wavelet transform algorithms [60]. Moreover, the segmentation accuracy of the proposed method is quite high. Comparison between obtained results and Dajnowiec *et al.* [74] (Dajnowiec combined multilevel thresholding with 3D region growing to obtain better performance) results on the same series of DICOM images has shown that the proposed method outperformed the algorithm in case of speed and accuracy. An example of this comparison is illustrated in figures 5.3(a). Since the proposed method uses edge information to segment the lung in CT images, the method may introduce an error if the slices get processed independently and a large portion of patient's lung was filled with large opacities in a way that the opacity connects cross borders of lung together as shown in figure 5.2(a) and (b). However, 3D rendering of lung or anatomical knowledge can be used to overcome drawback of processing slices independent of each others.

Most segmentation algorithms tend to have segmentation error where trachea or bronchi gets too close to the lung border. Distance between lung and airway tree can become to be only a few pixels and the soft tissue between airway and lung has indistinguishable profile as small vessels. Because of de-noising characteristic of wavelet transformation in its expansions, these tiny borders may be considered as noise and consequently ignored by

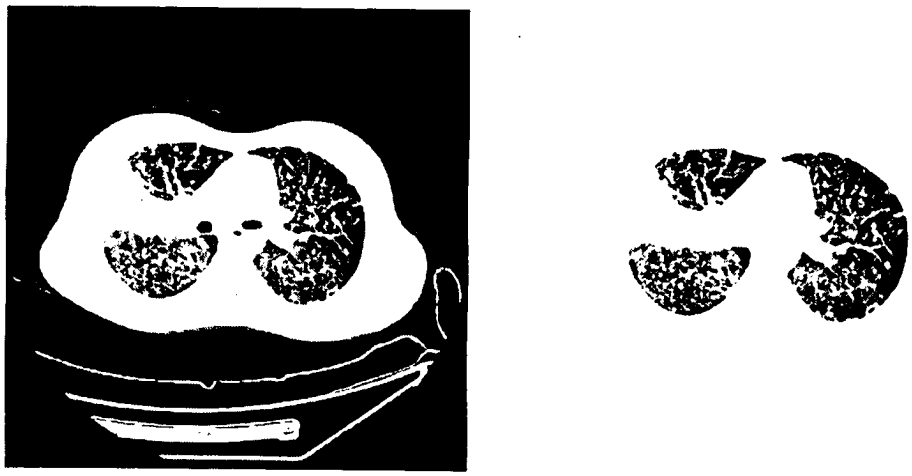

(a) (b)

**Figure 5.2:** (a) An original thorax image(b) its segmentation result.

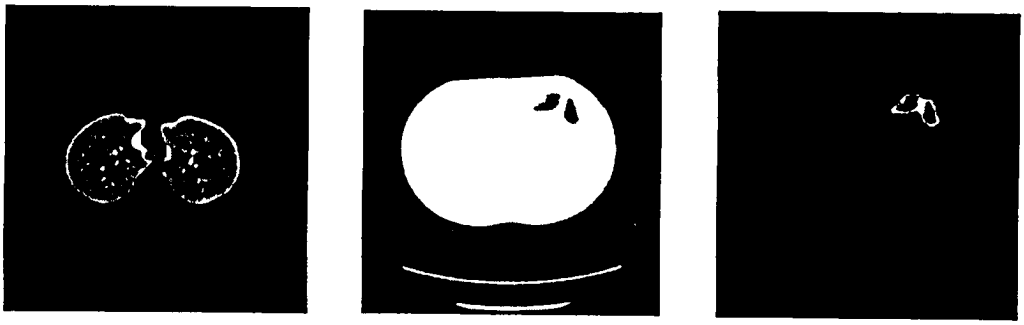

(a) (b) (c)

**Figure 5.3:** (a) An example of 3D segmentation result (the original thorax image shown in figure 5.4) (b) and (c) Bowel gas segmentation as result of watershed (slice forty eighth in the series).

algorithm. Therefore, trachea and main bronchi were extracted through the series and their edges ignored in the lung segmentation steps. Figure 5.4 shows a thoracic CT image with and without precursor trachea and main bronchia segmentation.

## 5.3 Automated Density Analysis in Dynamic CT

Dynamic Computed Tomography involves repeatedly imaging the organ of interest over time. It can generate a tremendous number of CT images for analysis with a single experiment. Manual segmentation of each image to be studied is very time consuming. Fast automatic segmentation of the lung and subsequent evaluation of its respective density is a prerequisite for any clinical application of this technique. Several studies have examined dynamic CT images of thoracic organs such as the heart [76, 77, 78] and solitary pulmonary nodules [79].

Acute Respiratory Distress Syndrome is a form of acute lung injury of multiple etiologies including pneumonia, sepsis, severe trauma and blood transfusions. Pathologically it is characterized by diffuse alveolar damage with epithelial and endothelial damage, pulmonary edema, inflammatory exudates and cellular proliferation. The typical CT appearance of ARDS is of bilateral ground-glass opacification with a gravity-dependent gradient and atelectasis/consolidation most commonly in the middle and basal parts of the lungs. The affected parts of the lung have increased attenuation compared to normal lung. An example of normal lung and lung affected by ARDS is illustrated in figure 5.5.

Dynamic CT with a cine loop technique was performed on a rabbit model with ARDS induced by repeated saline lavage. Dynamic CT was performed on an 8 detector multislice CT scanner (GE Lightspeed, GE Medical Systems, Milwaukee,WI). Imaging consisted of simultaneous acquisition of 4 slices (one volume) every 0.2 seconds. Images were acquired for just under 10 seconds producing 192 images per scan. The tube voltage was 120 kV and the tube current was 120 mA. A $512 \times 512$ matrix was used and the slice thickness was 5mm. The display field of view was 16cm. The voxel size was $0.3125 \times 0.3125 \times 5$mm with an average slice volume of $128cm^3$. Use of between 4 and 6 volumes of 4 slices each enabled imaging of the whole chest throughout the respiratory cycle. Therefore, each animal generated a dataset

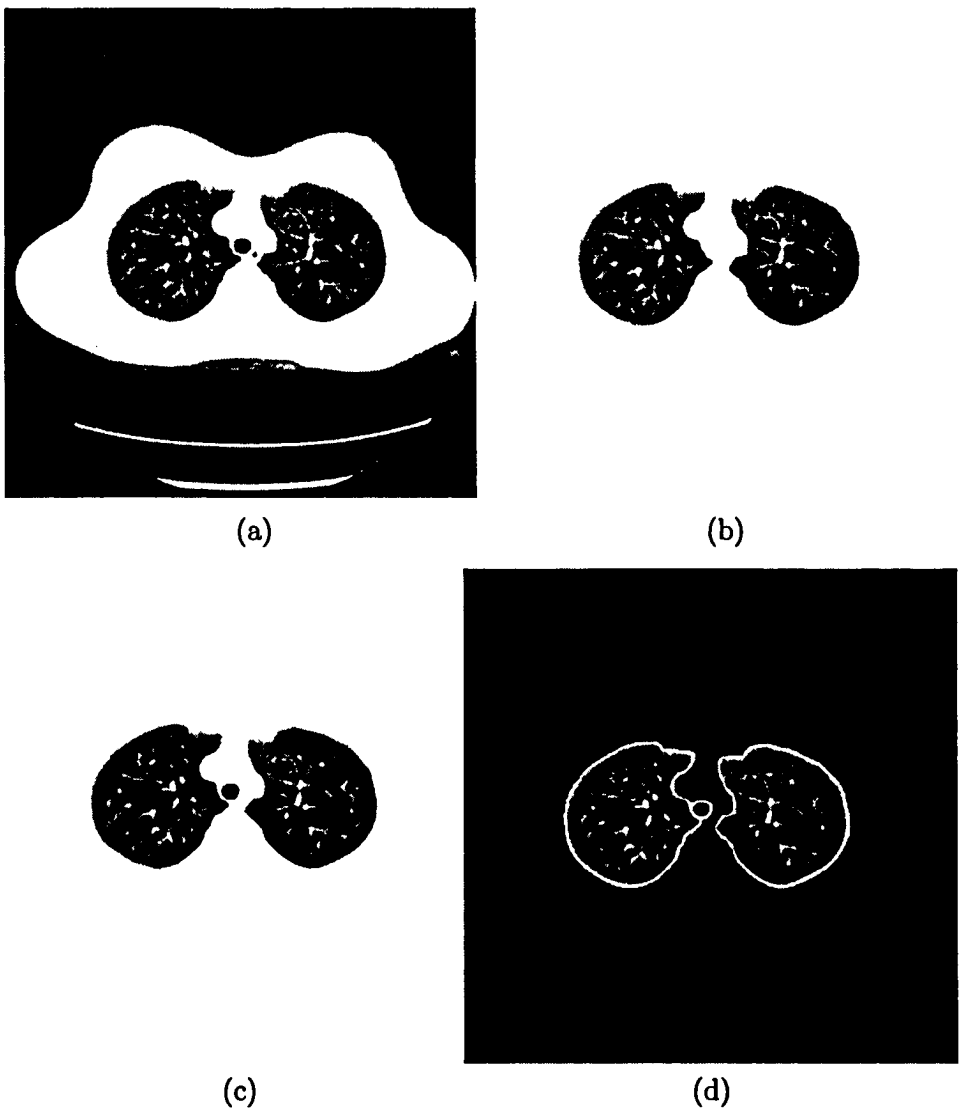


**Figure 5.4:** (a) Thorax CT image. (b) Segmentation result after airway extraction. (c) Segmentation result without precursor trachea and main bronchia extraction. (d) Extracted lung illustrated on black background.

(a) (b)

**Figure 5.5:** (a) Healthy lung (b) affected lung with ARDS.

of between 768 ($192 \times 4$) and 1152 ($192 \times 6$) images. Images were reconstructed using a bone detail algorithm for lung visualization. A series of selected images over a respiratory cycle are shown in figure 5.6.

The automatically segmented images were compared with manually segmented images obtained by an experienced radiologist to verify the accuracy of the proposed method. A close correlation was found between the segmentation results. The volume between these segmentations was calculated as the system error. The average segmentation error was calculated as $1mm^3$ in a respiratory cycle. For comparison purposes, the same CT slice was segmented using the wavelet transform software and an established image processing software developed for the MacIntosh computer (Osirix) (figure 5.8). The Osirix software performs segmentation using a 2D growing region algorithm. This requires user-defined upper and lower Hounsfield unit thresholds and placement of initial seed points within the lung. Where the two lungs are separated by the mediastinum, two seed points must be placed one for each lung. We found in lungs with ARDS, multiple different thresholds must be trailed to segment the lung effectively and different thresholds are needed depending on the distribution and severity of the ARDS. This means that using this software becomes time-consuming and labour-intensive and can only be described as semi-automatic. In contrast, our software is able to automatically segment the lung affected with ARDS with a high degree of accuracy even when the lung is densely consolidated.

A further processing step allowed calculation of the volumes occupied by ventilated lung (-900 to -500 HU) and atelectatic lung (-300 to 200 HU) over each respiratory cycle. An


**Figure 5.6:** The same thoracic level over a single respiratory cycle along with extracted lung consist of a series of 8 scans separated temporally by 0.4Sec.

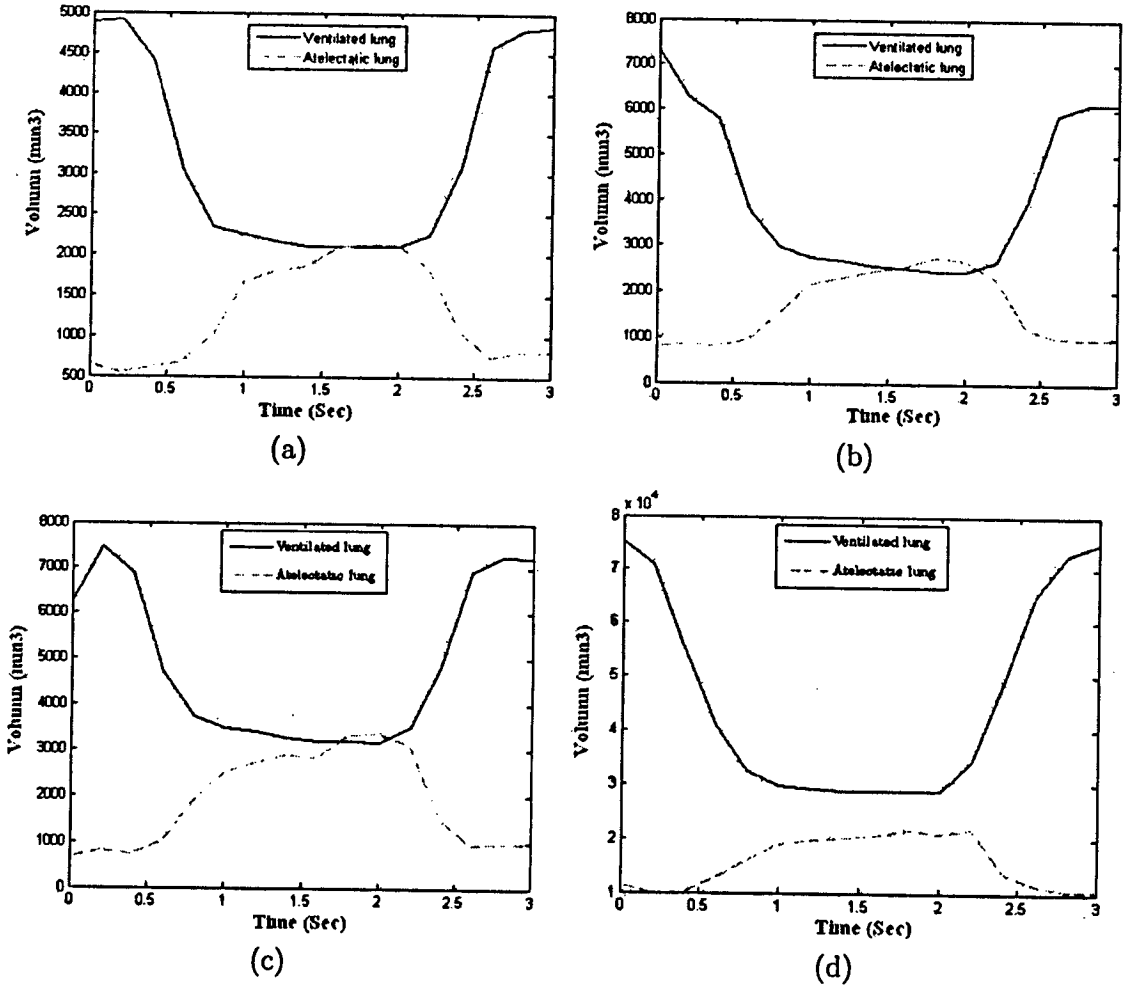


**Figure 5.7:** Calculation of the volumes occupied by ventilated lung and atelectatic lung over each respiratory cycle at each thoracic level (a, b, and c) and for the whole lung (d).

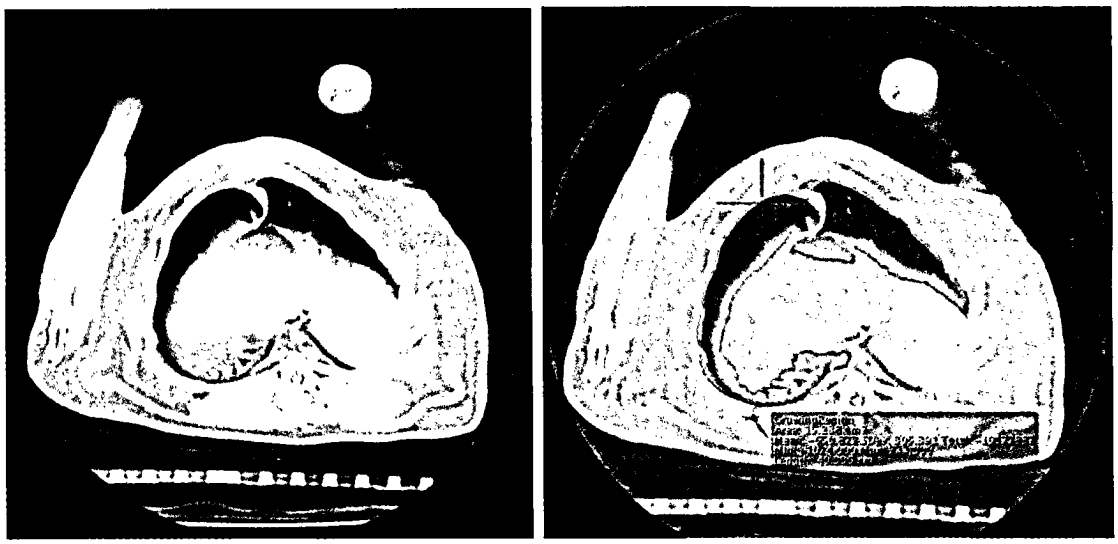

(a) (b)

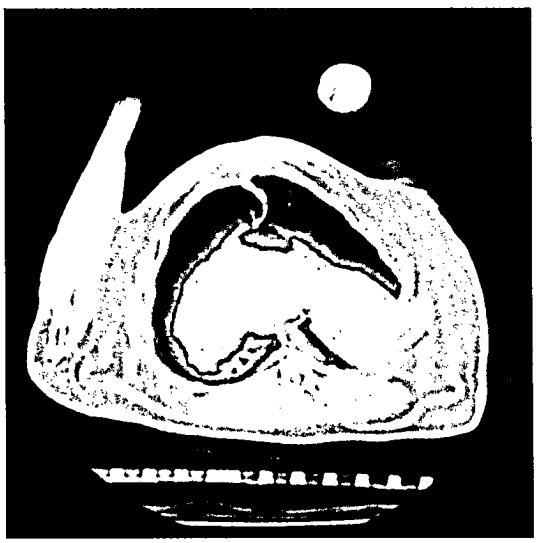

(c)

**Figure 5.8:** (a) Original thoracic image (b) Segmented by Osirix (c) segmented by the proposed method.

example of this analysis is illustrated in figure 5.7. This shows how the amount of atelectatic lung increases as expected towards expiration with a corresponding decrease in the amount of ventilated lung. In addition, with our technique the lung can be separated into user definable regions such as posterior and anterior subdivisions. Division of the lung into these subdivisions was made using the thoracic bones as anatomical landmarks. As a result of this regional dissection, the distribution of lung densities can be temporally evaluated in each subdivision. This demonstrates how temporal changes are more marked in the posterior subdivision of the lung.

Finally, lung density analysis was performed by calculating the number of voxels within each range of HUs multiplied by the volume of each voxel in the series. Selected results of density analysis at different thoracic levels are shown in figure 5.9.

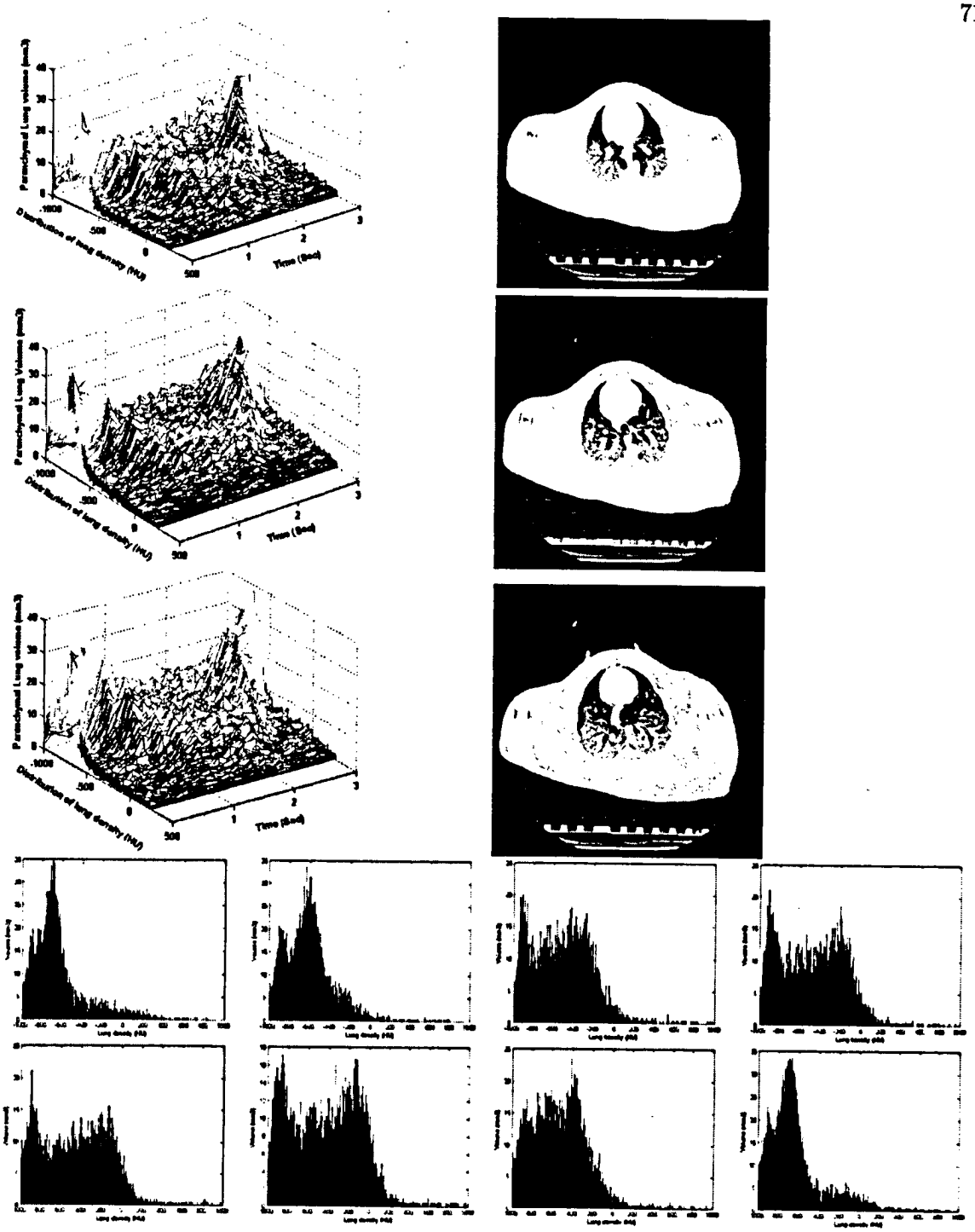

Figure 5.9: Analyzed density distribution of the lung over a respiratory cycle in 3 different thoracic levels along with corresponding image taken on peak expiration and histogram of selected images in figure 5.6.

# Chapter 6

# Conclusion and Future Work

## 6.1 Conclusion

The objective of the current research was to develope an automated computerized system to facilitate the diagnosis process for thoracic radiologists. The two main requirements for such a system are: the system has to provide low number of false positives per case and the system must have high sensitivity. To reach this goal, a collaboration between the Department of Electrical Engineering of Ryerson University and the Medical Imaging Department of the Toronto Hospital for Sick Children is established. A computer-aided diagnosis system is developed to detect the pulmonary lung nodules in CT images. The CAD system tends to outperform previously introduced methods in number of false positives and sensitivity measures. Nevertheless, the system may be modified to offer better performance in detection of pleural nodules in its later extensions in order to reduce the number of false positives.

A nodule enhancement filter is designed in order to eliminate the vessels before offering the data to the classifier module. The filter not only enhances the nodules in the series but also suppresses other structures including the blood vessels. This valuable step considerably reduces computational expenses, processing time, and the number of false positives in the CAD system. Basically the enhancement filter highlights region of interests for the classifier module and then the classifier module decides whether the emphasized region is an abnormal area or a normal one.

The initial step in processing an organ is segmenting the organ of interest in medical

images. A fast and reliable segmentation method is proposed through this thesis. Accuracy assessment of the segmentation method was done by comparing the segmentation result with manual segmentations of experienced radiologists. In addition to this the segmentation results of 220 CT images by this method is verified by a thoracic radiologist in prior to utilizing the proposed segmentation method in the CAD system. Achieving the objective of this research is fully depended on the accuracy of this step since any faulty segmentation may lead to missing a focal abnormality.

The pulmonary nodules, except pleural nodules, are seen as spherical objects while the vessels are tubular structures. An enhancement filter is introduced to emphasize on the spherical shaped objects inside the lung. This filter is based on the wavelet transformation and eigenvalues of the Hessian matrix at each point. Most false positives are reported to be the vessels. Employing this filter reduces the number of false positives dramatically. Basically, the filter avoids presenting the tubular structures (vessels) to the classifier. The classifier is responsible for classifying of the nodules from other region of interests in each thorax image. Various types of classifiers including neural network and LDA have been employed by researchers to perform a classification task. However, a least-squares support vector machine scheme is utilized in this research to perform such a classification task. Support vector machines are reported to provide better results in classification problems, especially when the problems are nonlinear such as the nodule detection problem. Least-squared support vector machine is preferred over the conventional SVM due to its simplicity and providing unique optimized values for each training set. Since the performance of LS-SVM is highly dependent on the provided training set, an assortment dataset of nodules are presented to the classifier. Upon employing this scheme it turns out that it is able to detect the nodules within an acceptable number of false positives per case as defined for a commercial CAD system used in a hospital with high level of sensitivity.

## 6.2 Future Works

A lung nodule detector CAD system was implemented through the course of this study. However, the current system can be improved to provide lower number of false positives and a higher true negative rate. The proposed system can be developed both in detecting region of interest, by improving the nodule enhancement filter to bring more sensitivity to unusual abnormalities cases, and the nodule classifier module. Nevertheless, growth of the gold standard dataset in number and variety provides better training set to the intelligence system and leads to robustness augmentation of the CAD system. The gold standard dataset must be acquired under a unique settings (scanner, does, axial resolution and etc.) to provide a better understanding of the nodules for the SVM classifier. Furthermore, a higher CT images quality can be achieved by imposing the requirements of the scanner, the radiation dose, the acquisition setup, reconstruction protocol and utilization of state-of-art scanners.

The proposed enhancement filter is downgraded from a 3D filter to a 2D filter due to the low axial resolution in the studied datasets acquired from children. This dimensional reduction decreases the filter sensitivity to some nodules which are entrapped between two adjunct blood vessels in two cases. This happens because of reduction in information as an effect of projection of 3D data into a 2D space by MIP. Processing datasets in which the axial resolution is close to the other direction's, provides an opportunity to employ the enhancement filter in its 3D form.

Combination of the proposed enhancement filter with another filter which enhances pleural tail nodules in the images, increases the performance of the system. The proposed enhancement filter is computationally expensive in a sense that it is based on eigenvalues of the Hessian matrix. Having employed a mother wavelet that discards the eigenvalue calculation of the matrices modestly reduced the computational expenses of the proposed CAD system.

Although all the pleural nodules were detected through this study, most of the FPs are introduced by soft tissues, including the connecting tissue of each lung lobes. Therefore, upgrading the methodology to detect the pleural nodules in this study may noticeably decrease

the number of FPs in each case study.

Quantitative CAD systems and Dynamic CT have many potential applications. As already discussed, it may be used to assess changes in lung attenuation with time which occur in ARDS and to assess the effect of different therapeutic interventions in this condition. Changes in lung attenuation may also be used to assess diseases in which air trapping is an important feature such as emphysema and asthma [80]. Similarly, in foreign body aspiration it may be used to infer the location of the foreign body by identifying a region of lung which does not change in volume with respiration. Dynamic CT can also be used to look at patterns of contrast enhancement with time. This may be useful in the characterization of solitary pulmonary nodules (benign vs malignant) [81] and has also been shown to enable the characterization of different types of pulmonary edema [82]. A further potential application of dynamic CT is the assessment of diaphragmatic movement which may be abnormal in both neurological disorders and respiratory disease. Finally, dynamic ventilation imaging with four-dimensional pulmonary CT has recently been proposed as a way of examining regional ventilation and as an aid to radiotherapy planning for lung cancer [83].

# Bibliography


[1] S. Diciotti, G. Picozzi, M. Falchini, M. Mascalchi, N. Villari, and G. Valli, "3d segmentation algorithm of small lung nodules in spiral CT images," 2007.

[2] K. Doi, "Current status and future potential of computer-aided diagnosis in medical imaging," *British Journal of Radiology*, vol. 78, pp. s3–s19, 2005.

[3] S. G. A. III, G. McLennan, M. F. McNitt-Gray, C. R. Meyer, D. Yankelevitz, D. R. Aberle, C. I. Henschke, E. A. Hoffman, E. A. Kazerooni, H. MacMahon, A. P. Reeves, B. Y. Croft, and L. P. Clarke, "Lung image database consortium: Developing a resource for the medical imaging research community," *Radiology*, vol. 232, pp. 739–748, 2004.

[4] R. T. Heelan, B. J. Flehinger, M. R. Melamed, M. B. Zaman, W. B. Perchick, J. F. Caravelli, and N. Martini, "Non-small-cell lung cancer: Results of the new york screening program," *Radiology*, vol. 151, pp. 289–293, 1984.

[5] W. J. Tuddenham, "Glossary of terms for thoracic radiology: recommendations of the nomenclature committee of the fleischner society," *American Jounal of Roentgenol*, vol. 143, pp. 509–517, 1984.

[6] A. J. H, M. N. L, and F. PJ, "Glossary of terms for CT of the lungs: recommendations of the nomenclature committee of the fleischner society," *Radiology*, vol. 200, pp. 327–331, 1996.

[7] W. J. Kostis, A. P. Reeves, D. F. Yankelevitz, and C. I. Henschke, "Three-dimensional

segmentation and growth-rate estimation of small pulmonary nodules in helical CT images," *IEEE Transactions on Medical Imaging*, vol. 22, pp. 1259–1274, 2003.

[8] H. Takizawa and S. Yamamoto, "Recognition of lung nodules from x-ray CT images using 3D markov random field models," in *16th International Conference on Pattern Recognition*, vol. 1, 2002, pp. 99–102.

[9] M. Antonelli, G. Frosini, B. Lazzerini, and F. Marcelloni, "A CAD system for lung nodule detection based on an anatomical model and a fuzzy neural network," in *Annual meeting of Fuzzy Information Processing Society*, 2006, pp. 448–453.

[10] C. Croisille, M. Souto, M. Cova, S. Wood, Y. Afework, J. E. Kuhlman, and E. A. Zerhouni, "Pulmonary nodules: Improved detection with vascular segmentation and extraction with spiral CT," *Radiology*, vol. 197, pp. 397–401, 1995.

[11] T. Tozaki, Y. Kawata, N. Niki, H. Ohmatsu, K. Eguchi, and N. Moriyama, "Three-dimensional analysis of lung area using thin slice CT images," in *Proceedings SPIE Medical Imaging*, vol. 2709, 1996, pp. 2–11.

[12] M. L. Giger, K. T. Bae, and H. MacMahon, "Computerized detection of pulmonary nodules in computed tomography images," *Investig. Radiology*, vol. 29, pp. 459–465, 1994.

[13] S. G. Armato, M. L. Giger, C. J. Moran, J. T. Blackburn, K. Doi, and H. MacMahon, "Computerized detection of pulmonary nodules on CT scans," *Radiographics*, vol. 19, pp. 1303–1311, 1999.

[14] K. Kanazawa, Y. Kawata, N. Niki, H. Satoh, H. Ohmatsu, R. Kakinuma, M. Kaneko, N. Moriyama, and K. Eguchi, "Computer-aided diagnostic system for pulmonary nodules based on helical CT images," *Computer-Aided Diagnosis Medical Imaging, K Doi, H MacMahon, M L Giger, and K Hoffmann, Eds. Amsterdam, The Netherlands: Elsevier*, pp. 131–136, 1999.

[15] M. Fiebich, C. Wietholt, B. C. Renger, S. G. Armato, K. R. Hoffman, D. Wormanns, and S. Diederich, "Automatic detection of pulmonary nodules in low–dose screening thoracic CT examinations," in *Proceddings Medical Imaging, SPIE*, vol. 3661, 1999, pp. 1434–1439.

[16] M. S. Brown, M. F. McNitt-Gray, J. G. Goldin, R. D. Suh, J. W. Sayre, and D. R. Aberle, "Patient-specific models for lung nodule detection and surveillance in CT images," *IEEE Transactions on Medical Imaging*, vol. 20, pp. 1242–1250, 2001.

[17] D.-T. Lin and C.-R. Yan, "Lung nodules identification rules extraction with neural fuzzy network," in *Proceedings of the 9th International Conference on Neural Information Processing*, vol. 4, 2002, pp. 2049–2053.

[18] S. G. A. 3rd, M. L. Giger, and H. MacMahon, "Automated detection of lung nodules in CT scans: Preliminary results," *Medical Physics*, vol. 28, pp. 1552–1561, 2001.

[19] S. G. Erberich, K. Song, H. Arakawa, H. K. Huang, W. Richard, K. S. Hoo, and B. W. Loo, "Knowledge-based lung nodule detection from helical CT [abstract]," *Radiology*, 1997.

[20] D. J. Vining, Y. Ge, D. K. Ahn, and D. R. Stelts, "Virtual colonoscopy with computer-assisted polyp detection," *Computer-Aided Diagnosis in Medical Imaging, K. Doi, H. MacMahon, M. L. Giger, and K. R. Hoffman, Eds. Amsterdam, The Netherlands: Elsevier Science B.V.*, pp. 445–452, 1999.

[21] R. M. Summers, C. F. Beaulieu, L. M. Pusanik, J. D. Malley, R. B. Jeffrey, D. I. Glazer, and S. Napel, "Automated polyp detector for CT colonography: Feasibility study," *Radiology*, vol. 216, pp. 284–290, 2000.

[22] R. M. Summers, C. D. Johnson, L. M. Pusanik, J. D. Malley, A. M. Youssef, and J. E. Reed, "Automated polyp detection at CT colonography: Feasibility assessment in a human population," *Radiology*, vol. 219, pp. 51–59, 2001.

[23] H. Yoshida and J. Nappi, "Three-dimensional computer-aided diagnosis scheme for detection of colonic polyps," *IEEE Transaction on Medical Imaging*, vol. 20, pp. 1261–1274, 2001.

[24] H. Yoshida, Y. Masutani, P. MacEneaney, D. T. Rubin, and A. H. Dachman, "Computerized detection of colonic polyps at CT colonography on the basis of volumetric features: Pilot study," *Radiology*, vol. 222, pp. 327–336, 2002.

[25] J. Nappi and H. Yoshida, "Automated detection of polyps with CT colonography: Evaluation of volumetric features for reduction of false-positive findings," *Academic Radiology*, vol. 9, pp. 386–397, 2002.

[26] G. Kiss, J. V. Cleynenbreugel, M. Thomeer, P. Suetens, and G. Marchal, "Computer-aided diagnosis in virtual colonography via combination of surface normal and sphere fitting methods," *European Radiology*, vol. 12, pp. 77–81, 2002.

[27] S. B. Gokturk, C. Tomasi, B. Acar, C. F. Beaulieu, D. S. Paik, R. B. Jeffrey, J. Yee, and S. Napel, "A statistical 3D pattern processing method for computer-aided detection of polyps in CT colonography," *IEEE Transaction on Medical Imaging*, vol. 20, pp. 1251–1260, 2001.

[28] B. Acar, C. F. Beaulieu, S. B. Gokturk, C. Tomasi, D. S. Paik, R. B. Jeffrey, J. Yee, and S. Napel, "Edge displacement field-based classification for improved detection of polyps in CT colonography," *IEEE Transaction Medical Imagine*, vol. 21, pp. 1461–1467, 2002.

[29] D. S. Paik, C. F. Beaulieuv, R. B. Jeffrey, G. D. Rubin, and S. A. Napel, "Detection of polyps in CT colonography: A comparison of a computer aided detection algorithm to 3D visualization methods [abstract]," *Radiology*, vol. 213P, 1999.

[30] Y. Lee, T. Hara, H. Fujita, S. Itoh, and T. Ishigaki, "Automated detection of pulmonary nodules in helical CT images based on an improved template-matching technique," *IEEE Transaction Medical Imaging*, pp. 595–604, 2001.

[31] J. Dehmeshki, X. Ye, M. V. CasiquE, and X. Y. Lin, "A hybrid approach for automated detection of lung nodules in CT images," in *3rd IEEE International Symposium on Biomedical Imaging*, 2006, pp. 506–509.

[32] L. Boroczky, L. Zhao, and K. P. Lee, "Feature subset selection for improving the performance of false positive reduction in lung nodule CAD," *18th IEEE Symposium on Computer-Based Medical Systems*, pp. 85–90, 2005.

[33] S. Diciotti, G. Picozzi, M. Falchini, M. Mascalchi, N. Villari, and G. Valli, "3D segmentation algorithm of small lung nodules in spiral CT images," *IEEE Transaction on information technology in biomedicine*, vol. 11, pp. 1–1, 2007.

[34] K. Suzuki, S. G. A. III, F. Li, S. Sone, and K. Doi, "Massive training artificial neural network (mtann) for reduction of false positives in computerized detection of lung nodules in low-dose computed tomography," *Medical Physics*, vol. 30, pp. 1602–1617, 2003.

[35] K. Heitmann, H. U. Kauczor, P. Mildenberger, T. Uthmann, J. Perl, and M. Thelen, "Automatic detection of ground glass opacities on lung HRCT using multiple neural networks," *European Radiology*, vol. 7, pp. 1463–1472, 1997.

[36] H. Arimura, S. Katsuragawa, K. Suzuki, F. Li, J. Shiraishi, S. Sone, and K. Doi, "Computerized scheme for automated detection of lung nodules in low-dose computed tomography images for lung cancer screening," *Academic Radiology*, vol. 11, pp. 617–629, 2004.

[37] V. Vapnik, *The Nature of Statistical Learning Theory.* New York: Springer-Verlag, 1995.

[38] J. Malone, J. M. Rossiter, S. Prabhu, and P. Goddard, "Identification of disease in CT of the lung using texture-based image analysis," in *Conference Record of the Thirty-Eighth Asilomar*, vol. 2, 2004, pp. 1620–1624.

[39] W. A. H. Mousa and M. A. L. I. Khan, "Lung nodule classification utilizing support vector machines," in *International Conference on Image Processing*, vol. 3, 2002, pp. 153–156.

[40] M. G. Penedo, M. J. Carreira, A. Mosquera, and D. Cahello, "Computer-adided diagnosis: A neural-network based approach to lung nodule detection," *IEEE Transaction on Medical Imaging*, vol. 17, pp. 872–880, 1998.

[41] J. Suykens, L. Lukas, P. V. Dooren, B. D. Moor, and J. Vandewalle, "Least squares support vector machine classifiers : a large scale algorithm," in *Proceedings of the European Conference on Circuit Theory and Design (ECCTD'99)*, 1999, pp. 839–842.

[42] R. Fletcher, *practical Methids of Optimization.* chichster and New York: John Wiley and Sons, 1950.

[43] J. A. K. Suyken and J. Vandewalle, "Least squares support vector machine classifiers," *Neural processing letters*, vol. 9, pp. 293–300, 1999.

[44] J. Nocedal and S. J. Wright, *Numerical Optimization.* Springer, 1999.

[45] J. Mercer, "Functions of positive and negative type and their connection with the theory of integral equations," *Philos. Trans. Roy. Soc. London*, vol. 209, pp. 415–446, 1909.

[46] R. C. Gonzalez and R. E. Woods, *Digital Image processing*, 2nd ed. Prentice Hall, 2001.

[47] S. Hu, E. A. Hoffman, and J. M. Reinhardt, "Automatic lung segmentation for accurate quantitation of volumetric x-ray ct images," *Medical Imaging, IEEE Transactions*, vol. 20, pp. 490–498, 2001.

[48] S. N. Yu and C. T. Chiang, "Similarity searching for chest CT images based on object features and spatial relation maps," in *Engineering in Medicine and Biology Society, EMBC*, vol. 1, 2004, pp. 1298–1301.

[49] Y. Itai, K. Hyoungseop, S. Ishikawa, S. Katsuragawa, K. N. T. Ishida, and A. Yamamoto, "Automatic segmentation of lung areas based on snakes and extraction of abnormal areas," in *Tools with Artificial Intelligence, ICTAI 05. 17th IEEE International Conference*, 2005, pp. 377–381.

[50] C. H. Chuang and W. N. Lie, "Region growing based on extended gradient vector flow field model for multiple objects segmentation," in *Image Processing, International Conference*, vol. 3, 2001, pp. 74–77.

[51] H. Tek and B. B. Kimia, "Image segmentation by reaction-diffusion bubbles," in *Fifth International Conference on Computer Vision (ICCV'95)*, 1995, pp. 156–162.

[52] L. Vincent and P. Soille, "Watersheds in digital spaces: an efficient algorithm based immersion simulations," *IEEE Transactions on Pattern Analysis and Machine Intelligence*, pp. 583–598, 1991.

[53] A. Witkin, "Scale space filtering," *Proc. 8th Int. Joint Conference Artifcial Intelligence*, pp. 1019–1022, 1983.

[54] S. G. Mallat and S. Zhong, *Complete signal representation with multiscale edges.* New York University Tech. Rep. No. 483, 1989.

[55] S. Mallat and W. L. Hwang, "Singularity detection and processing with wavelets," *IEEE Transaction on Information Theory*, pp. 617–643, 1992.

[56] X. Yansun, J. B. Weaver, D. M. Healy, and L. Jian, "Wavelet transform domain filters: A spatially selective noise filtration technique," *Image Processing, IEEE Transactions*, vol. 3, pp. 747–758, 1994.

[57] D. A. Karras and B. G. Mertzios, "On edge detection in MRI using the wavelet transform and unsupervised neural networks," in *Video/Image Processing and Multimedia Communications*, vol. 4th EURASIP Conference focused on Volume 2, 2003, pp. 461–466.

[58] Q. H. Lu and X. M. Zhang, "Multiresolution edge detection in noisy images using wavelet transform," in *Machine Learning and Cybernetics*, vol. 8, 2005, pp. 5235–5240.

[59] S. G. Mallat, "A theory for multiresolution signal decomposition: The wavelet representation," *IEEE Trans. Pa. Anal. Machine Zntell.*, pp. 674–693, 1989.

[60] S. Mallat and S. Zhong, "Characterization of signals from multiscale edges," *Pattern Analysis and Machine Intelligence*, vol. 14, pp. 710–732, 1992.

[61] D. Marr, *Vision.* San Francisco: W.H. Freeman, 1982.

[62] J. Canny, "A computational approach to edge detection," *IEEE Transactions on Pattern Analysis and Machine Intelligence*, vol. PAMI-8, pp. 679–698, 1986.

[63] T. Hara, M. Hirose, X. Zhou, H. Fujita, T. Kiryu, R. Yokoyama, and H. Hoshi, "Nodule detection in 3D chest CT images using 2nd order autocorrelation features," in *IEEE 27th Annual Conference on Engineering in Medicine and Biology*, 2005.

[64] K. Okada, D. Comaniciue, and A. Krishnan, "Robust anisotropic gaussian fitting for volumetric characterization of pulmonary nodules in multislice CT," *IEEE Transactions on Medical Imaging*, vol. 24, pp. 409–423, 2005.

[65] C. Lorenz, I. C. Carlson, T. M. Buzug, C. Fassnacht, and J. Weese, "Multi-scale line segmentation with automatic estimation of width, contrast and tangential direction in 2D and 3D medical images," in *First Joint Conference on Computer Vision, Virtual Reality and Robotics in Medicine, and Medical Robotics and Computer-Assisted Surgery Springer*, 1997, pp. 233–242.

[66] A. F. Frangi, W. J. Niessen, R. M. Hoogeveen, T. van Walsum, and M. A. Viergever, "Model-based quantitation of 3D magnetic resonance angiographic images," *IEEE Transaction on Medical Imaging*, vol. 18, pp. 946–956, 1999.

[67] Y. Sato, S. Nakajima, N. Shiraga, H. Atsumi, S. Yoshida, T. Koller, G. Gerig, and R. Kikinis, "3D multi-scale line filter for segmentation and visualization of curvilinear structure in medical images," *Medical Image Analysis*, vol. 2, pp. 143–168, 1998.

[68] Y. Sato, C. Westin, A. Bhalerao, S. Nakajima, N. Shiraga, S. Tamura, and R. Kikinis, "Tissue classification based on 3D local intensity structure for volume rendering," *IEEE Transaction on Visualization And Computer Graphics*, vol. 6, pp. 160–180, 2000.

[69] Y. Sato, S. Nakajima, N. Shiraga, H. Atsumi, S. Yoshida, T. Koller, G. Gerig, and R. Kikinis, "Three-dimensional multiscale line filter for segmentation and visualization of curvilinear structures," *Medical Image Analysis*, vol. 2, 1998.

[70] R. Sivaramakrishna, J. S. Birbeck, B. E. Higgs, R. M. Cothren, R. Parisky, and W. D. Boswell, "Computer-aided detection of lung cancer fromcomputed tomography images," *Technology Review Journal*, pp. 79–92, 2002.

[71] A. A. Farag, A. El-Baz, G. Gimel'farb, and R. Falk, "Detection and recognition of lung abnormalities using deformable templates," in *Proceedings of the 17th International Conference on Pattern Recognition*, vol. 3, 2004, pp. 738–741.

[72] M. Danjnowiec, "A context based automated system for lung nodule detection in CT images," Master's thesis, Departement of Electrical Engineering, Ryerson University, 2005.

[73] N. Memarian, "Computerized detection of lung nodules with an enahnced false positive reduction scheme," Master's thesis, Departement of Electrical Engineering, Ryerson University, 2006.

[74] M. Dajnowiec, J. Alirezaie, and P. Babyn, "An adaptive rule based automatic lung nodule detection system," in *Pattern Recognition and Image Analysis, Lecture Notes in Computer Science*, 2005, pp. 773–782.

[75] R. Shojaii, J. Alirezaie, and P. Babyn, "Automatic lung segmentation in CT images using watershed transform," in *IEEE International Conference on Image Processing, ICIP*, vol. 2, 2005, pp. II – 1270–3.

[76] S. Szpala, M. Wierzbicki, G. Guiraudon, and T. M. Peters, "Real-time fusion of endoscopic views with dynamic 3D cardiac images: A phantom study," *IEEE Transactions on Medical Imaging*, pp. 1207–1215, 2005.

[77] C. W. Chen and T. S. Huang, "Analysis of left ventricle global deformation based on dynamic CT data," in *11th IAPR International Conference on Pattern Recognition*, 1992, pp. 443–446.

[78] L. Gu, "Hybrid 3D heart segmentation from dynamic CT images," in *IEEE/EMBS International Summer School on Medical Devices and Biosensors*, 2004, pp. 67–70.

[79] N. Takagi, Y. Kawata, N. Niki, K. Mori, H. Ohmatsu, R. Kakinuma, K. Eguchi, M. Kusumoto, M. Kaneko, and N. Moriyama, "3D analysis of solitary pulmonary nodules based on contrast enhanced dynamic CT," in *International Conference on Image Processing*, 1999, pp. 416–420.

[80] R. Tanaka, S. Sanada, N. Okazaki, T. Kobayashi, M. Fujimura, M. Yasui, T. Matsui, K. Nakayama, Y. Nanbu, and O. Matsui, "Evaluation of pulmonary function using breathing chest radiography with a dynamic flat panel detector: primary results in pulmonary diseases," *Invest Radiol*, vol. 41, pp. 735–45, 2006.

[81] C. A. Yi, K. S. Lee, E. A. Kim, J. Han, H. Kim, O. J. Kwon, Y. J. Jeong, and S. Kim, "Solitary pulmonary nodules: Dynamic enhanced multi-detector row CT study and comparison with vascular endothelial growth factor and microvessel density," *Radiology*, vol. 233, pp. 191–199, 2004.

[82] C. Schueller-Weidekamm, E. Wassermann, H. Redl, M. Prokop, M. Zimpfer, C. Herold, P. Germann, and R. Ullrich, "Dynamic CT measurement of pulmonary enhancement

in piglets with experimental acute respiratory distress syndrome," *Radiology*, vol. 239, pp. 398–405, 2006.

[83] T. Guerrero, K. Sanders, E. Castillo, Y. Zhang, L. Bidaut, T. Pan, and R. Komaki, "Dynamic ventilation imaging from four-dimensional computer tomography," *Phys Med Biol*, vol. 51, pp. 777–791, 2006.